Summer 2002

Atomic force microscopy used to determine the Young's modulus of vascular smooth muscle cells

Samuel C. Lieber
New Jersey Institute of Technology

Recommended Citation

Lieber, Samuel C., "Atomic force microscopy used to determine the Young's modulus of vascular smooth muscle cells" (2002). *Theses*. 695.
https://digitalcommons.njit.edu/theses/695

ABSTRACT

ATOMIC FORCE MICROSCOPY USED TO DETERMINE THE YOUNG'S MODULUS OF VASCULAR SMOOTH MUSCLE CELLS

by

Samuel C. Lieber

The Young's modulus of cultured mouse and rat vascular smooth muscle cells (VSMC) was measured with an atomic force microscope (AFM). The AFM can image the three-dimensional structure of biological cells in a physiological environment enabling real-time biochemical and physiological processes to be monitored at a resolution similar to that obtained for the electron microscope (EM). Cellular mechanical properties were determined by indenting the cell's body, and analyzing the indentation data with classical infinitesimal strain theory. This calculation was accomplished by modeling the AFM probe as a cone, as well as a blunted cone. The blunted cone geometry fits the AFM force indentation data well and was used to calculate the Young's Modulus (E) of the respective VSMC cell body under various conditions. HEPES, a buffer solution commonly used to maintain pH in culture was found to alter the Young's Modulus (E) and the morphology of rat cells. Old mouse VSMCs had a higher Young's Modulus (E) than younger ones, with a clear change in cytoskeleton morphology. A change in cell body morphology was seen after application of drug treatment.

ATOMIC FORCE MICROSCOPY USED TO DETERMINE THE YOUNG'S MODULUS OF VASCULAR SMOOTH MUSCLE CELLS

by

Samuel C. Lieber

A Thesis
Submitted to the Faculty of
New Jersey Institute of Technology
In Partial Fulfillment of the Requirements for the Degree of
Master of Science in Mechanical Engineering

Department of Mechanical Engineering

August 2002

APPROVAL PAGE

ATOMIC FORCE MICROSCOPY USED TO DETERMINE THE YOUNG'S MODULUS OF VASCULAR SMOOTH MUSCLE CELLS

Samuel C. Lieber

8/6/02

Dr. Nadine Aubry, Thesis Advisor — Date
Professor and Chair of Mechanical Engineering, NJIT

08/06/02

Dr. Ernest S. Geskin, Committee Member — Date
Professor of Mechanical Engineering, NJIT

8/1/02

I. Joga Rao, Committee Member — Date
Assistant Professor of Mechanical Engineering, NJIT

BIOGRAPHICAL SKETCH

Author:	Samuel C. Lieber
Degree:	Master of Science
Date:	August 2002
Date of Birth:	
Place of Birth:	

Undergraduate and Graduate Education:

- Master of Science in Mechanical Engineering
  New Jersey Institute of Technology, Newark, NJ, 2002

- Bachelor of Science in Mechanical Engineering
  New Jersey Institute of Technology, Newark, NJ, 2001

Major: Mechanical Engineering

Presentations:

Lieber, S.C.
“Validation of a bench durability test for bioprosthetic heart valves,” Heart & Valve Mechanics Division of the American Society of Mechanical Engineers (ASME), International Mechanical Engineering Congress and Exposition, November 2001.

To Charles, Maria, Leah and Sarah Lieber for their patience, understanding, and support.
To the New Jersey Institute of Technology for giving me the opportunity to learn.

There is no expedient to which a man will not resort to avoid the real labor of thinking.
Sir Joshua Reynolds

This thesis is dedicated to the memory of Isaac and Lea Lieber, Samuele and Rosa Leo, and Niny Filomena.

ACKNOWLEDGEMENT

I would like to thank my thesis advisor Dr. Nadine Aubry for her valuable input and support throughout this project. I would also like to express my gratitude to Dr. Stephen Vatner for his support and guidance during this collaboration between the New Jersey Institute of Technology (NJIT) and the University of Medicine and Dentistry of New Jersey (UMDNJ). I would like to thank Dr. Ernest Geskin and Dr. I. Joga Rao for participating in my thesis committee. I would like to express my deepest appreciation to Dr. Xueyan Zhang and Dr. Jun Kawabe who made this project a success with their tireless efforts.

Special thanks to the Cardiovascular Research Institute at UMDNJ, directed by Dr. Stephen Vatner, and Dr. Nadine Aubry at NJIT for funding this project.

Also I would like to express my appreciation to Dr. David Kristol, Dr. Boris Khusid, and Dr. Shlomo Gabbay for their involvement in my development as a researcher.

TABLE OF CONTENTS

TABLE OF CONTENTS
(Continued)

TABLE OF CONTENTS
(Continued)

Chapter **Page**

LIST OF TABLES

LIST OF FIGURES

LIST OF FIGURES
(Continued)

LIST OF FIGURES
(Continued)

CHAPTER 1

INTRODUCTION

1.1 Objective

The objective of this work is to analyze the effect of both aging and chemical treatment on the morphology and mechanical properties of vascular smooth muscle cells (VSMC) cultured from mice and rats. The Young's Modulus will be determined by indenting cells with an atomic force microscope (AFM), and interpreting indentation results with classical infinitesimal strain theory. Two forms of the theory, one which considers conical indenter geometry of the probe, and another which accounts for the blunted tip will be conducted in order to determine which method better fits the AFM indentation data. The selected method will then be used to compare the stiffness of young and old cells as well as drug treated cells.

1.2 Background of Medical Problem

The cardiovascular system (cardio refers to the heart, vascular to the vessels) consists of a central pump, the heart, and a network of tubes (blood vessels). This system transports blood which nourishes cells, removes cellular waste, and helps to protect against infection [1]. When the heart contracts (systole), blood is pumped into the large arteries (aorta) and the carotid arteries which then expand. As blood flows out of these arteries into smaller ones throughout the body the large blood vessels (aorta and carotid arteries) then recoil back to the size they were prior to the heart contraction. As the arteries relax, the heart also relaxes and fills with blood in preparation for the heart expansion (diastole)

[2]. The large blood vessels then recoil as the heart fills with blood. The aorta and large vessels store approximately 50% of the left ventricular stroke volume during systole, and the elastic forces of the aortic wall push this volume to the peripheral circulation in diastole [3]. To this end, the systolic-diastolic action has an influence not only on the peripheral circulation but also on the heart. Therefore, the arterial mechanical properties are a major determinant of cardiovascular function and therefore of a person's well being.

1.3 Anatomy of Arteries

The arterial wall has three components: the intima, the media, and the adventitia (Figure1.1) [4].

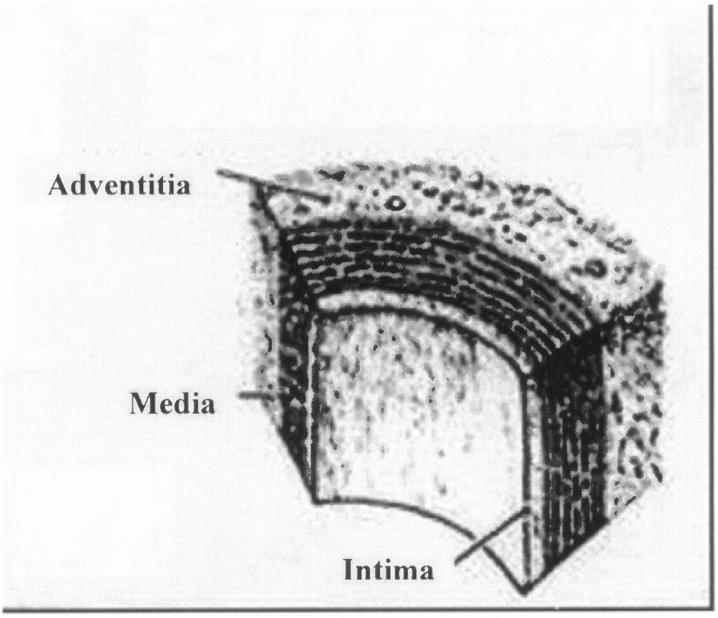

Figure 1.1 Anatomy of an artery with adventitia, media, and intima displayed [4].

The outermost covering of the arterial wall is called the adventitia, which is composed of connective tissue. The intima is the inner coat of the vessel closest to the blood flowing within the artery and consists of a single layer of endothelial cells. The media, or middle layer, is made up of vascular smooth muscle cells, which are surrounded by a network of collagenous and elastic fibers [4]. The media consists of a mesh of proteins (collagen and elastin), which form an extracellular matrix (ECM) in which vascular smooth muscle cells (VSMC) are embedded.

1.4 VSMC Role In Age Related Stiffening of Arteries

The age-related changes in vascular stiffness have been found to be risk factors for strokes and heart attacks, where the stiffness of the arteries determines the extent and rate of expansion and contraction of the arterial wall occurring during and after each heartbeat. The arterial stiffening is affected by both the VSMCs and the matrix proteins in the artery's makeup [2]. To this end, the medial layer, containing VSMCs embedded in an ECM, plays an important role in determining the mechanical properties of the arteries during aging [5]. The aging process affects arterial stiffness by causing cell death reducing the number of VSMCs in the arteries. The remaining VSMC's are forced to work harder causing them to enlarge. This change in morphology could lead to an increase in arterial stiffness [2]. There is increasing evidence that vascular stiffening due to aging can be slowed down by novel drugs. Accordingly, new therapeutic approaches targeting vascular stiffness have been proposed [6].

1.5 Atomic Force Microscopy

The atomic force microscope (AFM) can image the three-dimensional structure of biological cells in a physiological environment enabling real-time biochemical and physiological processes to be monitored at a resolution similar to that obtained for the electron microscope (EM). The process of image acquisition with the AFM probe allows forces to be measured at the molecular level [7]. Indentation of biological materials with the AFM tip provides detailed micromechanical properties of soft biological samples [8]. The indentation method existed prior to the development of the AFM and is a convenient test to assess the mechanical properties of solids. However, there are problems in interpreting the data originating from the complex geometry of the AFM probe. These problems increase as the indentation dimension is in the micro and nano indentation range [9]. Classical infinitesimal strain theory is a widely used approach to analyze the relationship between indentation force and depth. To this end, the preliminary results show that taking into account the tip geometry is necessary for the proper application of the classical infinitesimal strain theory in determining the mechanical properties of biological cells [8].

CHAPTER 2

LITERATURE SURVEY

2.1 Cell Structure and Mechanics

The mechanical properties of tissue cells may contribute to the overall deformation of the tissue under applied forces. The field of cell mechanics touches this topic as well as how cells move, deform, and interact, as well as how they sense, generate, and respond to mechanical forces. Recent developments in cell mechanics have included studies of cytoskeleton dynamics and cell-ECM interactions. These topics were examined as they relate to the shape, function, deformability, and mechanical properties of whole cells; and the viscoelasticity and connectivity of subcellular structures such as microtubules, actin filaments, and intermediate filaments [7].

The shape and mechanical properties of tissue cells likely depends on the cytoskeleton. The internal cytoskeleton is composed of an interconnected network of actin filaments (6–10 nm in diameter), intermediate filaments (7–11 nm) and microtubules (25 nm) [8]. The three filamentous systems of the cytoskeleton are believed to be the major stress-bearing components in the cell, but also could be the structures that provide the mechanical interconnections from the membrane to the nucleus [7]. The mechanical properties of the cytoskeleton are a determinant in cell shape, and cellular functions including spreading, crawling, polarity, and cytokinesis [9-13]. To this end, the microtubule assembly participates in diverse processes, such as cell morphology, cellular motility, intracellular organization and transport [14]. Microtubules can function as rigid struts opposing the force generated by actin/myosin interaction [14,15] and therefore may contribute to cytoskeletal stiffness [16,17].

2.2 AFM Development & Principle of Operation

The AFM, originally developed by Binning, Quate, and Gerber [18], can image the three dimensional surface structure of biological specimens. The AFM has been used to image living cells and the underlying cytoskeleton, chromatin and plasmids, ion channels, and a variety of membranes [19-24]. Dynamic processes such as crystal growth, mechanical pulses of cardiac cells, analysis of the mitotic cycle of living vertebrate cells, the polymerization of fibrinogen, and physicochemical properties such as elasticity and viscosity in living cells have been studied with the AFM [25-27].

The AFM tip, attached to a cantilevered spring, moves over the surface of the specimen and is deflected by the interaction forces between the tip atoms and the specimen atoms. Because the spring constant of the commonly used cantilevers (10^{-1} to 10^{-2} N/m) is much smaller than the intermolecular vibration spring constant of the atoms in the specimen (10 N/m), the cantilever can sense exquisitely small forces exerted by the individual sample atoms [25]. The deflection of the tip is a measure of the forces sensed by the cantilever. The sensed forces are transduced to develop molecular images. The sample is raster scanned in the xy-plane beneath the tip. The vertical position of the sample (z) is also monitored. These movements are controlled by a piezoelectric xyz scanner; the three coordinates are used to create the image [28].

2.3 AFM Cellular Imaging & Resolution

The AFM can image cellular and subcellular structures under physiological conditions with a resolution exceeding that of optical microscopes. Fixed erythrocytes dried onto glass cover slips were some of the first cells to be imaged by the AFM [19]; however, little information was obtained about the extracellular or intracellular structures. Living adult atrial cells were imaged at a resolution of ~20 nm [29]. At this increased resolution the cytoskeletal elements including muscle sarcomeres and cross bridges were able to be visualized [25]. Many cells have been imaged in aqueous conditions many of which have been alive [20,21,30-35].

The resolution obtained with the AFM may be cell dependent as well as hardware dependent. The limit of spatial resolution for AFM is not well defined. The images are formed by reconstructing the contour of forces exerted between the specimen and tip. By selecting a small scan size and appropriate operating conditions, one can often distinguish two adjacent objects that are < 1nm apart [36]. The lateral resolution in AFM is limited by the elastic indentation [37-41]. Biological materials, such as cells, often show a lower lateral resolution which can be explained by their deformation due to the AFM tip [38]. When the tip indents a soft surface, a certain contact area between the tip and sample is created. This contact radius can be taken as a measure of the lateral resolution if one ignores the surface roughness [37]. From elastic experiments, Radmacher et al. [41] calculated a diameter between 500 and 50 nm for this contact area which is in good agreement with the lateral resolution usually obtained on cells. Forces in the pN range (1-10 pN) are required to obtain high-resolution images on biological materials with about 1 nm vertical deformation and only a few nm^2 area of contact [38,39,42]. The lateral resolution is ~0.1 nm and is determined by the limitations of the hardware; the vertical resolution is 0.01 nm and hence can image molecular perturbations on the sample surface. The lateral resolution achieved depends on the characteristics of the tip, operating environment, and nature of the specimen [25].

For biological specimens in a normal imaging situation (such as imaging a living cell surface), the resolution is relatively poor (~10 nm) but higher than light microscopes and comparable with scanning electron microscopes. In the case of soft materials, such as cells, the achievable resolution will be limited by the elastic indentation of the sample by the tip. The resolution obtainable thus depends on the softness of the sample, the geometrical shape of the cantilever, and the loading force applied by the AFM tip [41]. The factor limiting resolution on the cell surface is the mobility of the upper membrane with respect to the lower membrane, which is anchored to the substrate, and also the mobility of the macromolecules within the membrane [25]. Improvements in resolution may be made by first increasing the surface rigidity by using suction of cells onto patch pipettes and thus reducing the lateral mobility; and second by imaging with low forces (attractive force mode imaging) [31].

Whole cell to molecule experiments in a physiological environment can be performed and dynamic changes in the molecular structure of channels, receptors, and other macromolecules can be seen [43]. AFM can be an important tool for growth and developmental studies of cells and processes such as nerve growth, synapse formation, and cell surface and cytoskeletal reorganizations [44]. Paul Hansma and coworkers [45] followed the polymerization of fibrinogen, a constituent of the ECM. This investigation was followed by the observation of other biological processes: the response of the cell membrane to a probing tip [21]; observation of the infection of a cell by viruses [46]; the imaging of living, human platelets during their activation [47], and the monitoring of slow motion on the surface of cells [48]. Other examples for following intracellular transport of material or changes of the underlying cytoskeleton of the AFM have been reported by several groups [21,44,48-51].

2.4 Forces Affecting AFM Probe

The sum of the forces on the tip causes the deflection of the cantilever; these forces can be attractive or repulsive. The forces acting on the tip vary depending on the mode of operation and the conditions used for imaging. In contact mode imaging, the tip is deflected, mainly due to repulsive forces from the overlapping electron orbitals between the tip atoms and the sample atoms. The dominant attractive force is a van der Waals force resulting primarily from the nonlocalized dipole-dipole interactions among atoms of the tip and specimen [18,52]. While imaging in fluids contributions from electrostatic Coulomb interactions between charges on the specimen and tip (either occurring naturally or induced because of polarization), osmotic pressure due to charge movements and rearrangements, and structural forces such as hydration force, solvation force, and adhesion force should be considered [25]. The manner in which the AFM generates images also make it an excellent sensor of molecular forces (hydrogen bonds, van der Waals and electrostatic forces) [53,54].

2.5 Measuring the Elastic Properties of Biological Material With The AFM

The elastic response of the cell is mainly due to its cytoskeleton [55,56]. The cytoskeleton is a network of three different polymeric proteins: actin, microtubules, and intermediate filaments, along with a large number of associated proteins that control assembly, disassembly, cross linking, and other properties of this filamenteous network [57]. The cytoskeleton is related to the cell shape, the change of this shape, and the self movement of the cells [9,58].

The principle of the cell poker is very similar to the method of using the AFM [59,60]. Other methods have been used to measure the entire cell's elastic properties including pipette suction method [61,62], flicker spectroscopy [63], and optical tweezers [64,65]. Bereiter-Hahn and coworkers used another scanning microscopy technique, scanning acoustic microscopy, to measure the elastic properties of cells locally [66,67]. The main difference between AFM and these techniques is the high lateral resolution (100 nm) provided by the AFM with the potential to increase with improved tip design [41].

AFM data can be interpreted as elasticity measurements [68-71]. The AFM allows the mechanical properties of biomolecules to be determined accurately from force-versus-distance curves (force curves) [72,73]. The relationship between indentation force and depth depends upon the tip geometry and the mechanical properties of the specimen [74]. Measuring the elastic properties of biological material with the AFM has been pioneered by Lindsay [71] who investigated the difference of bone and bone marrow, and by Weisenhorn [38] who investigated rubber, cartilage, and living cells. If the sample is soft the tip will deform it, and elastic indentation occurs. The force versus indentation curves becomes non-linear for softer samples, because the compliance of the sample becomes higher for larger loading forces. Radmacher considers the geometry of AFM tips to be conical, on a scale of several 10's to 100s of nm [41]. The contact area of the probe increases with indentation, the force-depth relationship in any soft material is nonlinear, making it difficult to assess how much of the response is due to the tip geometry [74]. Since, the contact area will increase while loading, indenting the sample. This process has been treated analytically by Hertz, where a relationship between the indentation and the loading force is given for smooth parabolic indenter profiles [75]. Most investigators have attributed nonlinearity of the indentation response entirely to the tip geometry, and have applied equations based on classical infinitesimal strain theory to extract the Young's modulus (E) of the material [38,76].

2.6 Classical Infinitesimal Strain Theory Applied To Indentation Problem

The indentation problem was originally solved by Hertz [75] for smooth parabolic indenter profiles and by Love [77] for conical indenters for which the Hertz theory does not apply [78]. The classical infinitesimal strain theory is a widely used approach because of the simple form of the theoretical equations [74]. The theory assumes that the sample is a homogeneous, isotropic, linear elastic half-space subject to infinitesimally small strains. Each of these key assumptions is questionable for AFM indentation studies in biological specimens. First, at the macroscopic level most biological materials are heterogeneous, anisotropic, and exhibit nonlinear constitute behavior [4]. This could pertain to the microscopic level as well. Second, in order to obtain an adequate indentation response with AFM, soft biomaterials typically need to be indented 50-500 nm, which is not infinitesimal compared to either the thickness of the sample (<2μm) or to the size of the indenter tip (~5-60 nm radius of curvature) [79,80]. Although, the AFM measures on a microscopic scale, the classical theory may still be reasonable because the tip indents 100 or more atoms on the surface [81].

The classical infinitesimal strain theory also indicates that pyramidal and conical indenters should have a semi-angle (α) close to 90 degrees [78] so that the gradient of displacement (strain) at the contact surface remains small (Figure 2.1).

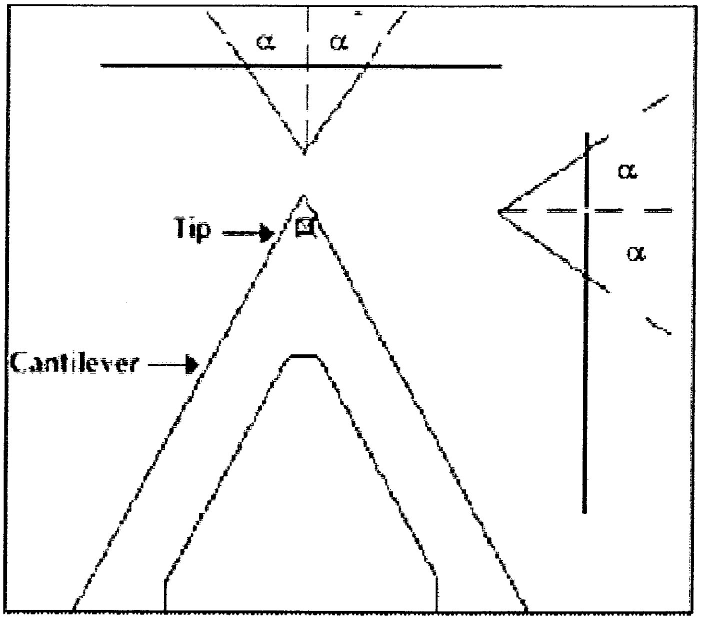

Figure 2.1 Cantilever tip with semi-angle α indicated.
Image courtesy of Digital Instruments, Santa Barbara CA.

AFM tips typically have an α value of 35 degrees. For indenters such as those used for AFM where $\alpha<45$, the strains are likely to be large in the vicinity of the indenter, even for small indentations relative to the sample thickness [80]. Thus, AFM indentation is more properly classified as a finite indentation problem, and analyses based on infinitesimal strain theory may be inappropriate.

Infinitesimal strain theory requires an infinitely large specimen relative to both the indentation depth and indenter size [78]. Indenter geometry relates to this issue because it determines the radius of contact between the indenter and the sample. A conical indenter, in theory, yields an indentation response that closely approximates that of commercially available silicon nitride (Si_3N_4) AFM Probes, the geometry of which is actually a four sided pyramid [79]. For cylindrical indenters, the contact radius is constant yielding a linear force-depth relation for infinitesimal indentations [82-84]. Nonlinearities arise when either the radius or indentation depth are larger than a certain fraction of the sample thickness [85,86]. For flat ended circular cylindrical probes which may not fully pertain to AFM tips, the following guidelines were established for indentation tests. The in-plane dimensions relative to the indenter size should be greater than 15, otherwise the effects of finite sized boundaries will need to be accounted for; the thickness-to-indenter size ratio should be greater than 10 to avoid nonlinearities and/or incorrect results due to finite thickness effects; and the thickness to indentation ratio should be greater than 5 to avoid the properties of the underlying substrate affecting the indentation results [86].

For a conical indenter, the indentation force-depth relation is always nonlinear because the contact radius increases with indentation depth .In contrast indentations with a blunt cone approached the theoretical solution for a small indentation with respect to thickness even for nonlinear materials and a semi-angle (α) less than 45 deg [74], because in this limit the indentation depth and contact radius are smaller than the spherical tip radius as required by infinitesimal theory [78].

Costa [74] demonstrated that the two critical factors determining the accurate assessment of elastic properties by indentation are whether the deformations are infinitesimal and whether the material exhibits linear or nonlinear characteristics. Applying infinitesimal theory incorrectly to finite-deformation situations can result in large errors in the estimation of material properties. Correctly accounting for finite indentations and the geometry of the indenter to calculate an apparent elastic modulus, may reveal material nonlinearity and heterogeneity [74]. However, Some researchers consider that the absolute determination of the Young's modulus of a biological sample is not always necessary, where only a comparison between two different states is needed [81].

2.7 Theoretical Analysis of Classical Infinitesimal Strain Theory With Conical & Blunt-Tipped Indenter Geometry Applied

In applications such as AFM, the indenter tip does not terminate in a point but instead is truncated in some way. Costa [74] used finite element models (FEM) to simulate a blunt cone indenter indenting into three materials. (with α=37.5 degrees) which merged smoothly into a spherical tip with a radius R=30 nm simulating an AFM probe. For an indentation (d) to thickness (t) ratio greater than 15% the cone and blunted cone data matched within ±10 %; however, for smaller indentations there was a distinction.

Nonlinear materials indented with an ideal cone resulted in the theoretical modulus overestimating the apparent one. In contrast, with a blunt cone indenter the apparent modulus approached the theoretical one as d/t approached zero. Thus using a blunt cone may allow more accurate quantitative estimates of some elastic properties of a material.

2.8 Measuring the Elastic Properties of Biological Material With The AFM

The Young's modulus is the basic material coefficient of elasticity. It can range from 100 GPa for hard materials (glass, steel) to 100s MPa for typical polymers (polystyrene), and 1 MPa for soft gel-like materials [41]. Typical values for cells are somewhere between 1 kPa and 200 kPa [24,38,41]. In order to accurately derive Young's modulus (E), the characteristics of the tip such as the tip radius, the cone angle, and force constant should be carefully estimated [79,87-89]. Also, the tip deformation should be negligible. In the case of Si_3N_4 tips, the modulus of Young is 150 GPa [38,90] and for commercial silicon cantilevers Young's modulus is 169 GPa (according to Digital Instruments). The supporting sample (glass substrates) is crucial too, because it is often used as a reference sample appearing hard compared to biomolecules. Glass itself is softer than the Si_3N_4 tip with a Young's modulus of 50 GPa and has a spring constant of about 50 N/m [38].

The elastic response of living and fixed cells has been reported qualitatively in the work by Schoenberger and Hoh [91] and in the work of Lal and coworkers [29].Weisenhorn et al. [38] were the first to measure the elastic properties of a living cell, and were the first to quantify the elastic behavior of cells from force curves and obtained a Young's modulus of 0.013-0.15 MPa for a living (lung carcinoma) cell. Radmacher and coworkers [24] were the first to determine quantitatively the elastic properties of cells as a function of the AFM position on the cell, where the Young's moduli ranged from 1 to 50 kPa (Hertz' model) [24]. Radmacher's correlation observed between the position on the platelet and the changing elastic modulus is an interesting observation, which was shown to be related to the underlying cytoskeleton [82]. However, a sizeable discrepancy was observed between the experimental data and simulations on the basis of Hertz' model. Micromechanical measurements performed on cultured rat atrial myocytes also showed a similar dependence of the elastic modulus on the position on the cell [Shroff, 1995]. Young's modulus in a nuclear region of the cell was 0.5-0.67 MPa (Ca2+-free solution, Sneddon mechanics), and increased 5-8-fold toward the periphery. These variations in stiffness could be related to the cytoskeletal heterogeneity [29]. According to Costa [75] the correct classical infinitesimal strain theory equations [38,83] have been misreported in several AFM publications [23,24,77,93]. Therefore, the mechanical properties of biological samples determined in previous work may be suspect.

CHAPTER 3

MATERIALS AND EXPERIMENTAL METHODS

3.1 Vascular Smooth Muscle Cell Culture

Mice and rats were killed in the age and drug treatment experiments respectively. The age study involved young (3 months) and old (2 years) female mice. The drug (nocodazole) and HEPES treatment studies involved female rats, where non-treated animals are labeled as a control. The aortic medial layer was isolated from the adventitia and the VSMC cultured as described previously [92,93]. A segment of the descending thoracic aorta was removed without stretching or compressing the tissue. The media was isolated by mechanical separation of extima and intima layers. The VSMCs were obtained using an enzyme digestion method from the media of the thoracic aorta. The isolated VSMCs (1×10^5 cells per well) were fed with DMEM containing 10% fetal bovine serum for 24 hours to allow attachment and then incubated in serum-free DMEM for 48 hours. The cultures incubated at 37°C and 95% humidity in air atmosphere containing 5% CO2. When most of the cells attached and spread on the cover glass, the cells were used for the AFM study.

3.2 Atomic Force Microscope Operation

The AFM (Figure 3.1) probes the surface of a sample with a sharp tip, a couple of microns long and often less than 100 A in diameter. The tip is located at the free end of a cantilever that is 100 to 200 μm long. Forces between the tip and the sample surface cause the cantilever to bend, or deflect. A detector measures the cantilever deflection as the sample is scanned under the tip. The measured cantilever deflections allow a computer to generate a map of surface topography (Figure 3.2) [25].

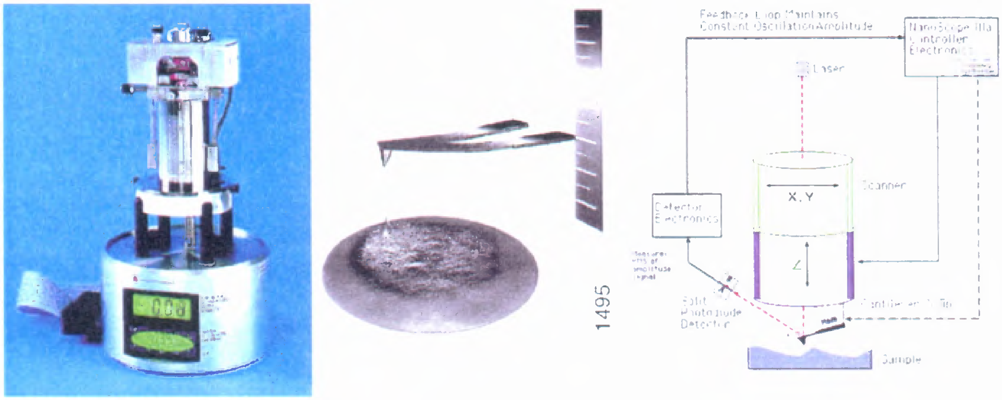

Figure 3.1 NanoScope® MultiMode™ AFM to the left. Cantilever and schematic of AFM operation to the right. Images Courtesy of Digital Instruments, Santa Barbara CA.

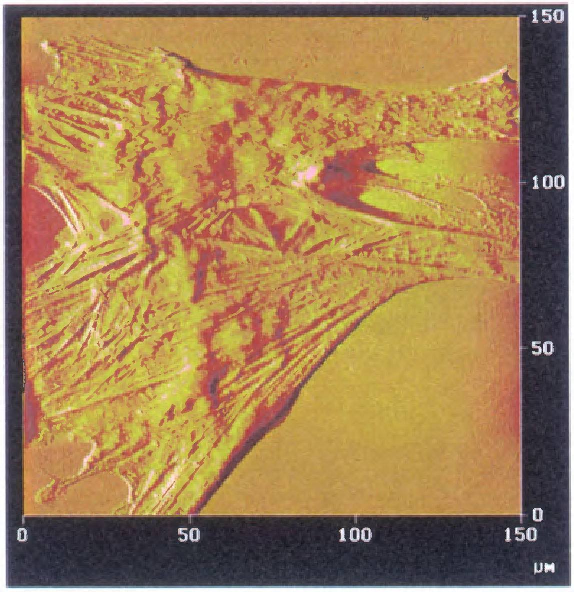

Figure 3.2 150 µm AFM scan of monkey VSMC, performed at the New Jersey Institute of Technology (NJIT) Keck Laboratory.

The force most commonly associated with atomic force microscopy is an interatomic force called the van der Waals force. The AFM can produce a force (P) vs. z-distance (D_z) curve, which is a plot of the deflection of the cantilever versus the extension of the piezoelectric scanner, measured using position-sensitive photodetector (PSPD). Local variations in the form of the P vs. D_z curve indicate variations in the local elastic properties. In the linear region of the P vs. D_z curves, the slope is related to the elastic modulus of the system [28].

3.3 Contact Mode AFM

In contact-AFM mode, an AFM tip makes soft physical contact with the sample. The tip is attached to the end of a cantilever with a low spring constant, lower than the effective spring constant holding the atoms of the sample together. As the scanner traces the sample under the tip, the contact force causes the cantilever to bend to accommodate changes in topography.

3.3.1 Constant Height Contact Mode AFM

The spatial variation of the cantilever deflection can be used directly to generate the topographic data set because the height of the scanner is fixed as it scans. Often used for taking atomic scale images of atomically flat surfaces where the cantilever deflections and thus variations in applied force is small. This method is also essential for recording real-time images of changing surfaces, where high scan speed is essential.

3.3.2 Constant Force Contact Mode AFM

The deflection of the cantilever can be used as input to a feedback circuit that moves the scanner up and down in the z direction, responding to the topography by keeping the cantilever deflection constant. An image is generated from the scanner's motion. With the cantilever deflection held constant, the total force applied to the sample is constant. This mode is generally preferred for most applications [94].

3.4 Tapping Mode AFM

A tapping mode technique involves oscillating the cantilever near its resonant frequency as it is scanned over the sample surface. The probe is brought closer to the sample surface until it begins to intermittently contact ("tap") on the surface. This contact with the sample causes the oscillation amplitude to be reduced. The oscillation's amplitude scales in direct proportion to the average distance of the probe to the sample as soon as the tip taps on the surface [94].

3.5 Non-Contact AFM

The non-contact (NC) AFM technique allows the probe tip to oscillate above the surface, thereby measuring the change in amplitude, phase, or frequency of the oscillating cantilever in response to force gradients from the sample. This is one of several vibrating cantilever techniques in which an AFM cantilever is vibrated near the surface of a sample. The spacing between the tip and the sample for NC-AFM is on the order of tens to hundreds of angstroms. This spacing corresponds to the non-contact regime on the van der Waals curve. The system vibrates a stiff cantilever near its resonant frequency (typically from 100-400 kHz) with amplitude of a few tens to hundreds of angstroms. It then detects changes in resonant frequency or vibration amplitude as the tip comes near the sample surface. The sensitivity of this detection scheme provides sub angstrom vertical resolution in the image, as in the contact AFM mode. Changes in the resonant frequency of the cantilever can be used as a measure of changes in the force gradient, which reflect changes in the tip-to-sample spacing, or sample topography. Non-contact AFM does not suffer from the tip or sample degradation effects that are sometimes observed after taking numerous scans with contact AFM. NC-AFM is also preferable to contact AFM for measuring soft samples. An AFM operating in contact mode will penetrate the liquid layer to image the underlying surface, whereas in non-contact mode an AFM will image the surface of the liquid layer [94].

3.6 Fluid Cell Operation

The imaging of samples in fluid is a growing facet of AFM technology. This method is prompted by a desire to observe biological specimens in their natural, fluid environments. The procedure for observing samples in fluid is the same as that for contact or Tapping Mode AFM in air; however, special hardware is utilized to contain the fluid (see Appendix A for operation procedures) [95].

3.7 Force Imaging With The AFM

A force plot is an observation of tip-sample interactions, which yields information regarding the sample. The Force Plot command in the View / Force Mode / Plot menu allows the microscopist to check the interaction between cantilever and sample. In Force

Plot mode, the X and Y voltages applied to the piezo tube are held at zero while a triangular waveform is applied to the Z piezo tube. As a result of the applied voltage, the cantilever tip moves up and down relative to the sample. The Z scan start parameter sets the offset of the piezo travel (its starting point), while the Z scan size parameter defines the total travel distance of the piezo. Therefore, the maximum travel distance is obtained by setting the Z scan start to +220 volts, with the Z scan size set to 440 volts. As the piezo moves the tip up and down, the cantilever-deflection signal from the photodiode is monitored. The force curve, a plot of the cantilever deflection signal as a function of voltage applied to the piezo tube, shows on the display monitor. A force plot in contact AFM is shown (Figure 3.8). What is occurring in the deflection versus z-position can be described as follows (Force Imaging Information From Digital Instruments Support Note 228E-Force Imaging) [96]:

- Piezo extends; tip descends.No contact with surface yet (Position 1).
- Tip is pulled down by attractive forces near surface (Position 2).
- As the tip presses into the surface, cantilever bends upward (Position 3).
- Piezo retracts; tip ascends until forces are in equilibrium with surface forces, and the cantilever relaxes downward (Position 4).
- Piezo continues retraction; tip ascends further. The cantilever bends downward as surface attraction holds onto the tip (Position 5).
- As the tip continues its ascent, the tip finally breaks free of surface attraction. The cantilever rebounds sharply upward (Position 6).
- As the piezo continues retracting, tip continues its ascent and no further contact with surface occurs during this cycle (Position 7).

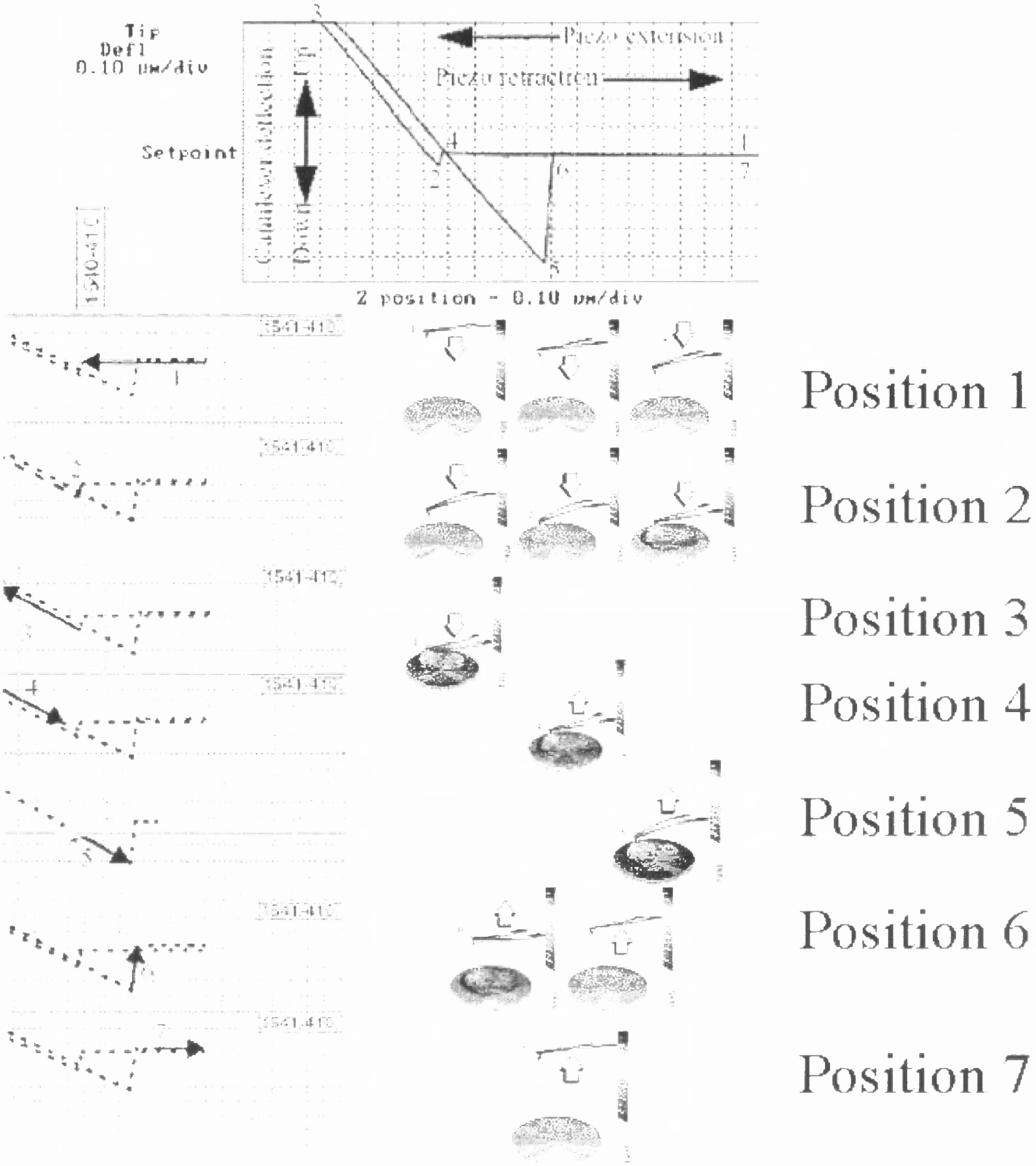

Figure 3.3 AFM force plot description. Sample image courtesy of Digital Instruments, Santa Barbara CA.

3.8 Calculating The Contact Force

The force curve shows the relationship between the setpoint and the deflection of the cantilever. Because the setpoint defines the value of the deflection signal maintained by the feedback loop, the force curve can be used to calculate the nominal contact force of the tip on the sample if the spring constant, of the cantilever, is known. The contact force is defined by the equation $P = k\Delta Z$, where ΔZ is the distance from the control point to V_{CSmin} in nanometers. Local variations in the form of the F versus the z-piezo distance (D_z) curve indicate changes in the local elastic properties. In the linear region of the P vs. D_z curves, the slope is related to the elastic modulus of the system [97].

3.9 Determining The Spring Constant (k) of The Cantilever

The cantilever's spring constant can be determined through experiments and also through theoretical calculations. Theoretical methods rely on knowledge of the cantilever's geometry and material properties (Young's elastic modulus (E) and Poisson's ratio (ν)) [98-101]. Static and dynamic experimental methods exist. Static methods utilise the deflection experienced by a cantilever when a constant known force is applied to the cantilever [102-104]. Dynamic methods focus on the dynamic behaviour of a cantilever, which includes measurement of the thermal response of the cantilever, and measurement of the change in resonant frequency caused by the addition of known masses to the cantilever [105-107]. The results utilised Paul Hansma's (University of California, Santa Barbara) calculations of spring constants for the four standard cantilevers found on SiNi substrates based on calculation methods presented by Sarid [108]. The spring constants are calculated based upon a thickness of 0.6 µm. The spring constants for SiNi cantilevers are shown in Table 3.1.

Table 3.1 Spring Constants For SiNi Cantilevers

Size (µm)	**Spring constant, K (N/m)**
100, wide	0.58
200, wide	0.12
100, narrow	0.38
200, narrow	0.06

All AFM experiments involved 200µm narrow SiNi probes with a 20-60 nm Radius Probe Tip (see Table 3.2 for specifications).

Table 3.2 Silicon Nitride Probe Specifications

Force (or Spring) Constants	0.58, 0.32, 0.12, 0.06 N/m*
Nominal Tip Radius of Curvature	20 - 60nm
Cantilever Lengths	100 & 200µm
Cantilever Configuration	V-shaped
Reflective Coating	Gold
Shape of Tip	Square Pyramidal
Tip Half Angle	35°

To this end, a spring constant of 0.06 N/m was used for calculations [97].

3.10 Acquiring Force-Distance Plots And Height Measurements With The AFM On VSMC

The technique used to acquire Force-Distance Plots with the AFM is illustrated in Figure 3.4.

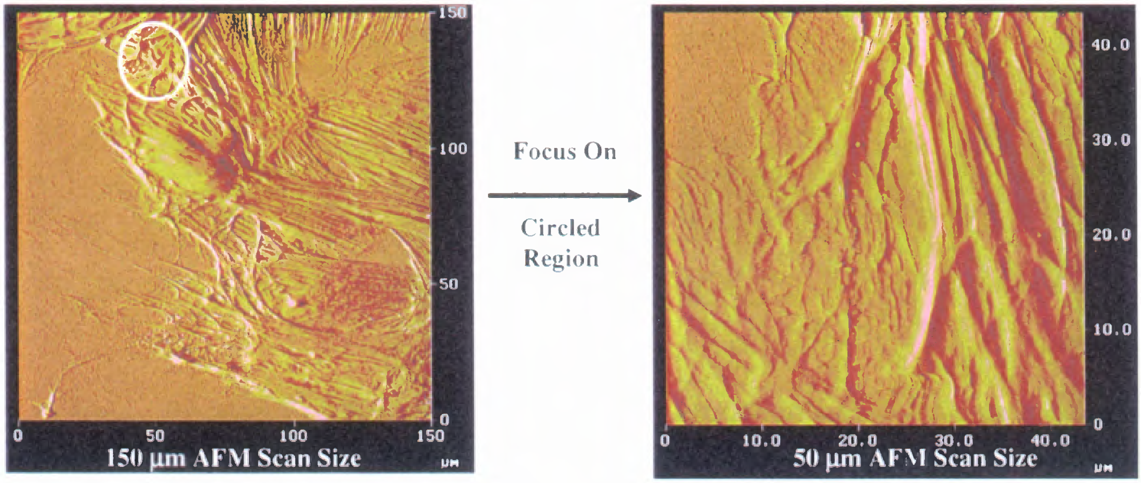

Thickness Measured In Circled Region

Force-Distance Plot In Circled Region

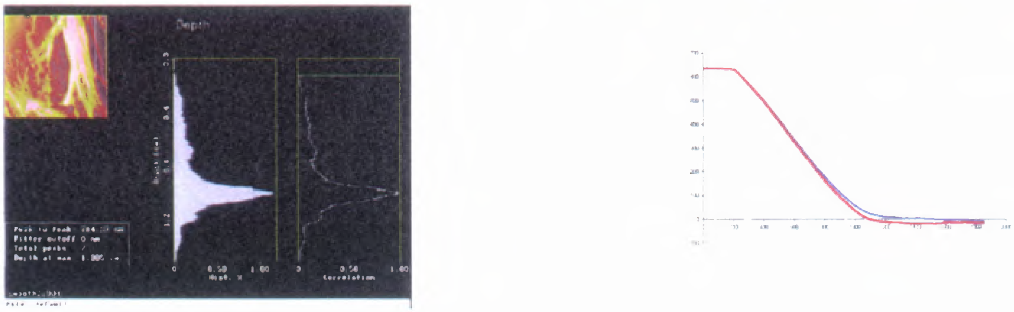

Figure 3.4 Technique for acquiring a Force-Distance plot and measuring thickness using an AFM on VSMCs. Performed at the New Jersey Institute of Technology (NJIT) Keck Laboratory.

The VSMC is first imaged at the AFM's maximum scan size (150 μm). A section of interest on the VSMC is selected for a closer examination. A force-distance plot is then constructed in this smaller section and the thickness of the cell body in this region is measured with the AFM software. The force-distance plot data is analyzed using classical infinitesimal strain theory.

3.11 Analysis Of Force Distance Curves With Classical Infinitesimal Strain Theory

Classical infinitesimal strain theory is a widely used approach [74]. The fundamental assumptions of the theory are that the sample is a homogeneous, isotropic, linear elastic half-space subject to infinitesimally small strains. These are the assumptions we have made regarding the cell-body material.

The following is the general equation for the total force (P) exerted by an indenter for infinitesimal indentations perpendicular to the finite stretch for the case of linear hyperelastic materials (see Appendix B for development of formulae) [74,83].

$$P=\frac{4}{3}\cdot E\cdot \pi \cdot \phi(d) \tag{3.1}$$

Here, E is Young's modulus and $\phi(d)$ is a function of the indenter geometry, which determines the dependence of P on the penetration depth d. The indentation problem can be solved for different indenter geometries by developing the appropriate $\phi(d)$ and inserting it into (3.1). We now consider $\phi(d)$ developed for the cone and blunted cone indenter shapes used in this analysis.

A cone with tip angle 2α is represented by the following function (see Appendix A for development of the function and Figure B.1) [77,83].

$$\phi(d)=\frac{2\cdot\tan(\alpha)}{\pi^2}\cdot d^2 \tag{3.2}$$

A blunt cone with tip angle 2α, which transitions at radius R (see Appendix A for development of the function) [109]. A blunted cone with a smooth transition from the cone to the spherical tip has the following relationship for b, $b=R\cos(\alpha)$.

For $d < b^2/R$, $\phi(d)$ is given by a sphere with radius R.

$$\phi(d)=\frac{4}{3\cdot\pi}\cdot\sqrt{R\cdot d^3} \tag{3.3}$$

For $d \geq b^2/R$, $\phi(d)$ is given by

$$\phi(d)=\frac{2}{\pi}\cdot\left[a\cdot d-\frac{a^2}{2\cdot\tan(\alpha)}\cdot\left(\frac{\pi}{2}-\operatorname{asin}\left(\frac{b}{a}\right)\right)-\frac{a^3}{3\cdot R}+\sqrt{a^2-b^2}\cdot\left(\frac{b}{2\cdot\tan(\alpha)}+\frac{a^2-b^2}{3\cdot R}\right)\right] \tag{3.4}$$

where the radius of contact a is derived from Equation 3.5 found in Reference [109]

$$d+\frac{a}{R}\cdot\left(\sqrt{a^2-b^2}-a\right)-\frac{a}{\tan(\alpha)}\cdot\left(\frac{\pi}{2}-\operatorname{asin}\left(\frac{b}{a}\right)\right)=0 \tag{3.5}$$

A Newton's method [110] was applied to (3.5) with a tolerance of $1E^{-15}$ in order to find the radius of contact a.

CHAPTER 4

RESULTS AND DISCUSSION

4.1 Comparison of Cone and Blunt-Cone Indenter Geometry Applied To Classical Infinitesimal Strain Theory

Control rat VSMCs were raster scanned in the xy-plane beneath the tip at 150 μm and 50 μm in contact mode with the AFM (Figure 4.1). In contact mode imaging, the tip was deflected, mainly due to repulsive forces from the overlapping electron orbitals between the tip atoms and the VSMC atoms. The sensed forces are transduced to develop images which are formed by reconstructing the contour of forces exerted between the VSMC and tip [28,36].

The shape and mechanical properties of tissue cells likely depends on the cytoskeleton [8]. The mechanical properties of the cytoskeleton are a determinant in cell shape, and cellular functions [9-13]. The cell body and nucleus are seen in Figure 4.1. The cellular and subcellular VSMC structures were imaged under physiological conditions with a resolution exceeding that of optical microscopes. The cell body shape was then measured in terms of thickness to be 424 nm.

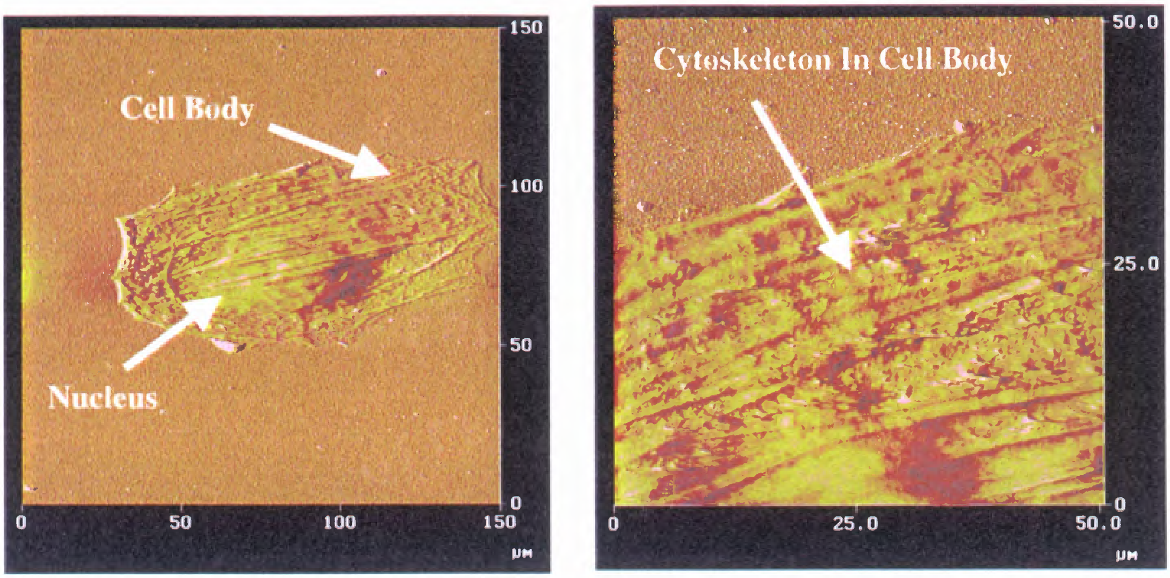

150 µm AFM Scan Size

50 µm AFM Scan Size

Figure 4.1 Control rat VSMCs imaged at 150 µm and 50 µm scans. From the 50 µm scan a Force Distance plot was measured and the thickness of the cell body was measured to be 424 nm.

The internal cytoskeleton (Figure 4.1) is composed of an interconnected network of actin filaments, intermediate filaments, and microtubules [8]. The three filamentous systems of the cytoskeleton are believed to be the major stress-bearing components in the cell, but also could be the structures that provide the mechanical interconnections from the membrane to the nucleus [7]. The microtubule assembly participates in diverse processes, such as cell morphology, cellular motility, intracellular organization and transport [14]. Microtubules can function as rigid struts opposing the force generated by the actin/myosin interaction [14,15] and therefore may contribute to cytoskeletal stiffness[16,17].

The cell body was indented to 100% of its thickness (424 nm) and a Force (P) Distance (D_z) plot was produced (Figure 4.3). The deflection of the tip is a measure of the forces sensed by the cantilever, and the vertical position of the sample (z) is monitored. A P-D_z plot is produced by plotting the deflection of the cantilever against the vertical position of the sample. The P-D_z plot appears typical of soft biological material as previously published [29,74,111,112].

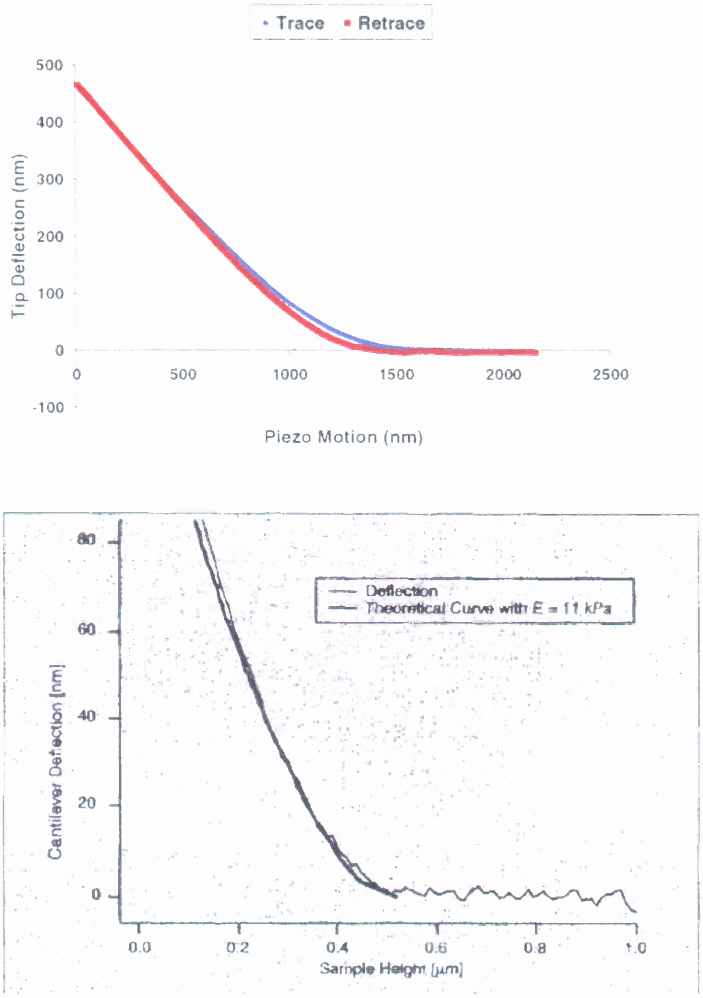

Figure 4.2 Force Distance plot (top) of control rat VSMC's cell body compares favorably to published Force Distance plots for biological materials (bottom) [41].

The trace portion of the P-D_z plot was analyzed for the Young's modulus (E). The approaching part (trace) of the P-D_z curve should always be used for calculating the indentation. The retracting part leads to wrong measurements of the indentation, because of adhesive forces [81]. The sample was indented 150 nm, because the AFM requires an indentation between 50-500nm to produce a proper P-D_z plot [74]. The Force Indentation graph (Figure 4.3) compares well to previously published theoretical and experimental curves for biological cells [29,74,111,112]. The relationship between indentation force and depth depends upon the tip geometry and the mechanical properties of the VSMC [74]. The contact area of the probe increases with indentation and the force-depth relationship in any soft material is nonlinear [74]. Investigators have attributed the nonlinearity of the indentation response entirely to the tip geometry, and have applied equations based on classical infinitesimal strain theory to extract a young's modulus of the material [38,76]. The classical infinitesimal strain theory is a widely used approach because of the simple form of the theoretical equations [74]. The fundamental assumptions of the theory are that the sample is a homogeneous, isotropic, linear elastic half-space subject to infinitesimally small strains. Each of these key assumptions is questionable for the AFM indentation study on VSMC samples. The VSMCs could be heterogeneous, anisotropic, and exhibit nonlinear constitute behavior [4].

The cell was also indented 150 nm which is not infinitesimal compared to the cell body thickness (424 nm) or the size of the indenter tip (20-60 nm radius of curvature) [79,80]. To this end, AFM indentation is more properly classified as a finite indentation problem, and these analyses based on infinitesimal strain theory may be inaccurate.

However, the classical theory may still be reasonable because the tip indents 100 or more atoms on the surface [81].

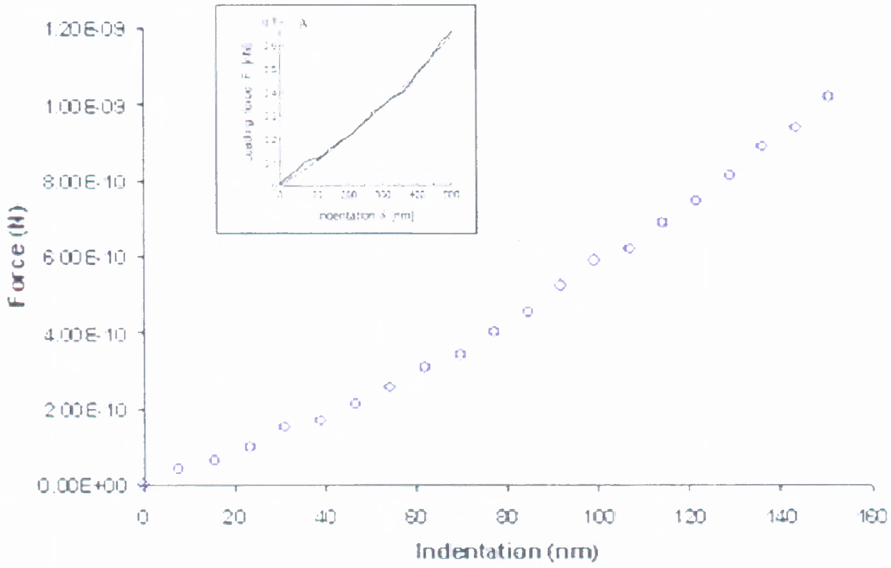

Figure 4.3 Force Indentation plot of control rat VSMCs imaged indented 150nm out of a cell body thickness of 424 nm (36% of thickness) compares favorably to published force-indentation plots (inner graph) [112].

Infintesimal strain theory requires an infinitely large specimen relative to both the indentation depth and indenter size [66]. Indenter geometry relates to this issue because it determines the radius of contact between the indenter and the sample. The Force-$4/3\pi\phi(d)$ graph (Figure 4.4) was produced with the cone and blunt cone indenter geometry in order to determine the Young's modulus from the slope of the best fit straight line [112]. A conical indenter, in theory, yields an indentation response that closely approximates that of commercially available silicon nitride (Si_3N_4) AFM Probes, the geometry of which is actually a four sided pyramid, but using a blunt cone may allow more accurate quantitative estimates of some elastic properties of a material [74,113] . Figure 4.5 demonstrates that the blunt cone geometry model fits the Force Indentation data better than the conical indenter model. The use of the conical indenter model gives a larger Young's modulus (E) calculated to be 76 % greater than the blunted geometry. (Figure 4.6). For a conical indenter, the indentation force-depth relation is nonlinear because the contact radius increases with indentation depth [74]. In contrast indentations with a blunt cone could fit the force indentation data better because the contact radius is small as required by infinitesimal theory [66].

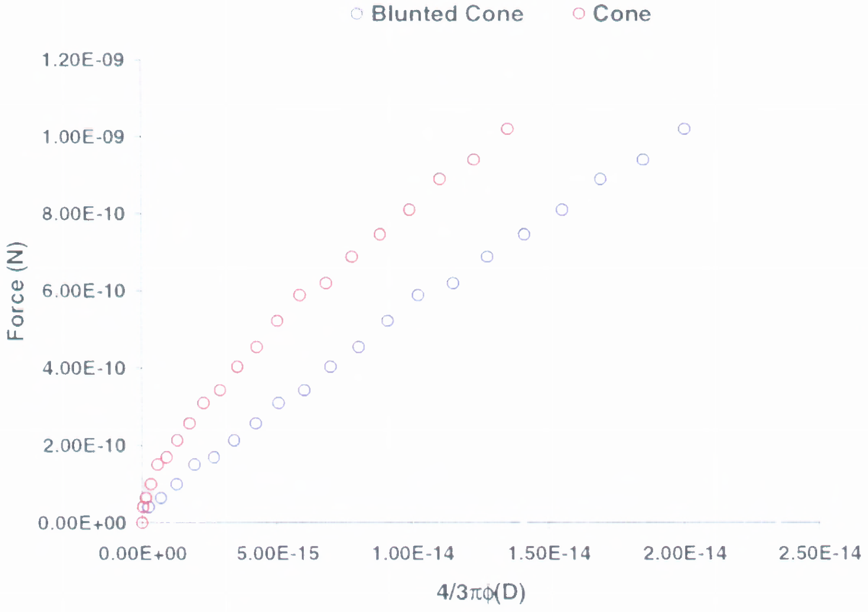

Figure 4.4 Force-4/3πϕ(d) graph for 150 nm indentation produced with the cone (red) and blunt cone (blue) indenter geometry in order to determine the Young's modulus from the slope of the best fit line.

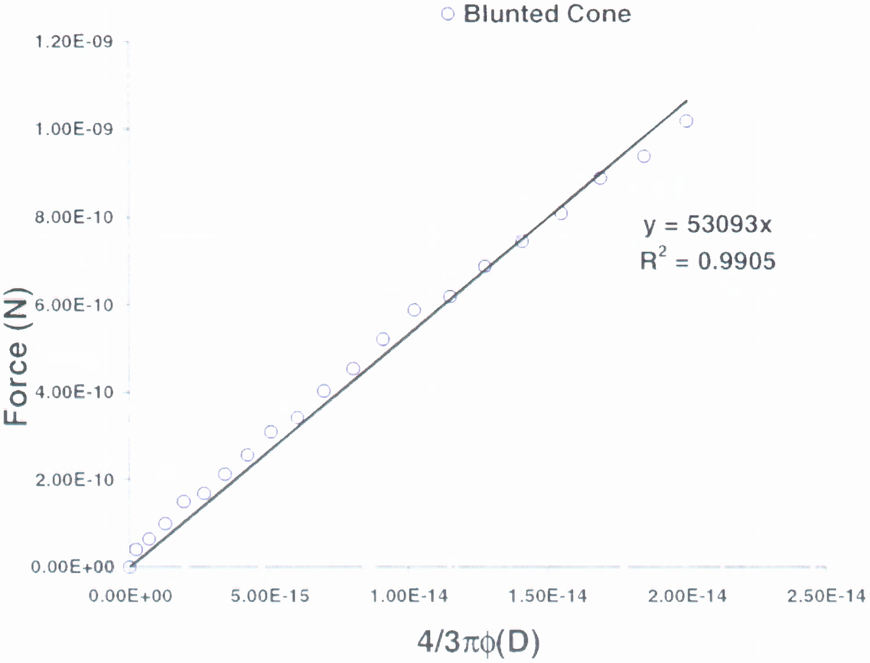

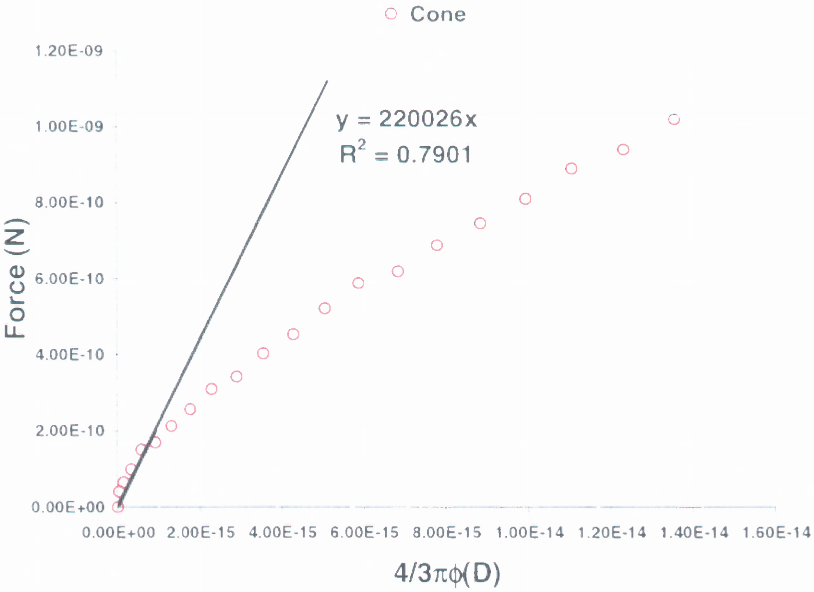

Figure 4.5 Best fit straight line applied to Force-4/3πϕ(d) graph for 150 nm indentation with the cone (red) and blunt cone (blue) indenter geometry. The Young's modulus is the slope of the trendline equation.

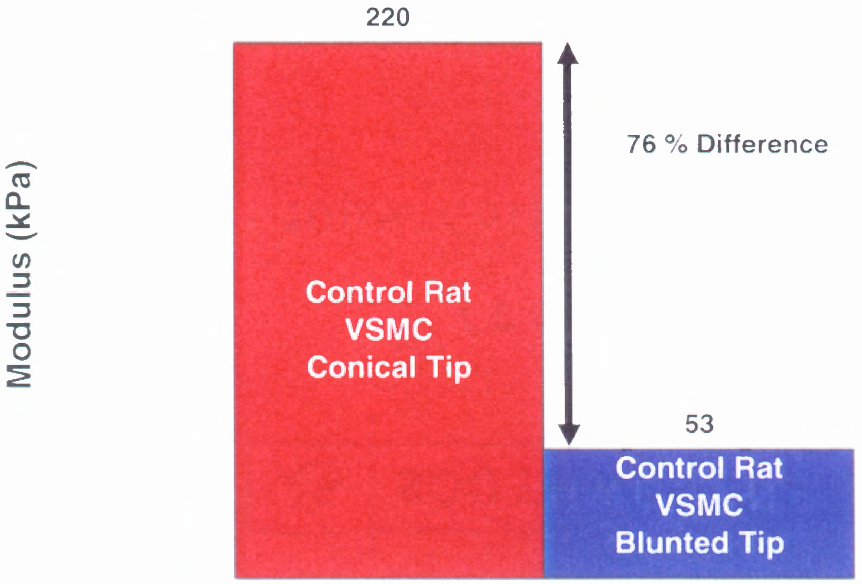

Figure 4.6 Comparison of the Young's modulus (E) determined from the slope of the trendline equation using the conical and blunted cone indenter geometries. A significant difference in Young's modulus (E) of 76 % is seen, where the conical model gives a larger Young's modulus.

4.2 Comparison of Young's Moduli Between HEPES (Buffer Treated) & Control Rat VSMCs

HEPES is a buffer solution known to regulate the pH of culture media [114]. HEPES is commonly used in cell culture applications. However, the exact effect of HEPES on the morphology and mechanical properties on the cell is not well understood. AFM images (Figure 4.7) clearly show the effect of the addition of HEPES on the cytoskeleton of the VSMC.

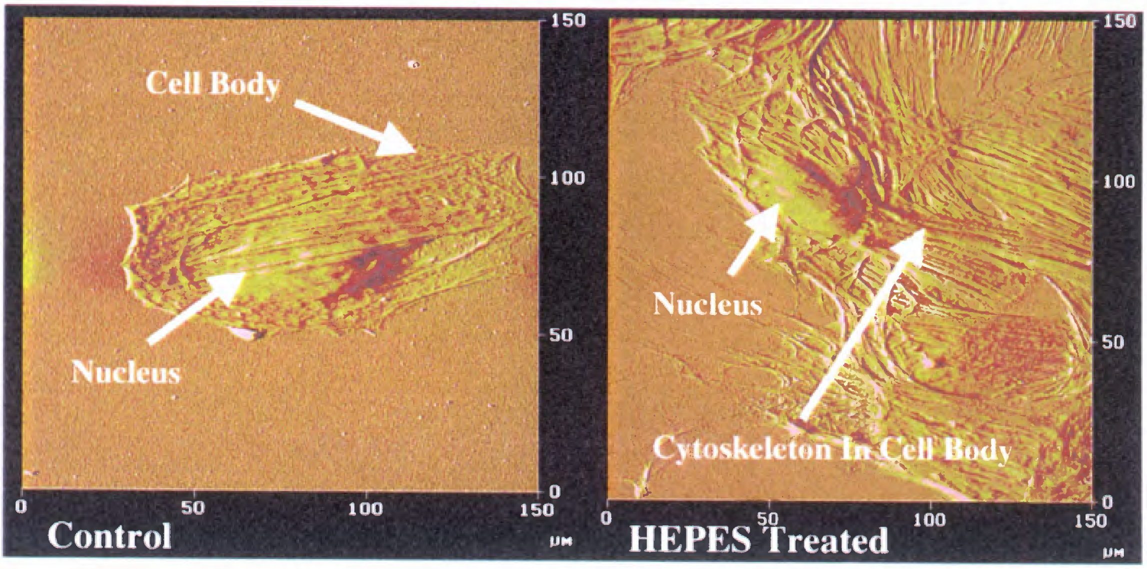

Figure 4.7 Comparison of control and hepes treated rat VSMC's. Note the increase in cytoskeleton fibers in the cell body as a result of HEPES addition.

The morphology change is clearly seen when HEPES buffer is added to the cultured VSMC. The change in thickness of the cell body was measured with the AFM. The cell body height of the HEPES treated cell was measured to be 1 µm, whereas the non-treated cell body height was 424 nm. This information was used in the development of a Force (P) Distance Plot (D_z). From this data, a blunt cone indenter geometry was used to compare the Young's modulus (E) for the HEPES treated and control cell (Figure 4.8) respectively, where E for the HEPES treated VSMC is smaller than that of the control cell by 23 %. The moduli values of 53 kPa and 41 kPa for the control and HEPES treated cell fall in the range of values (0-200 kPa) noted by other researchers for biological material [41]. This result has to be confirmed with another trial. However, in light of these results we did not use HEPES in our aging and drug treatment studies respectively.

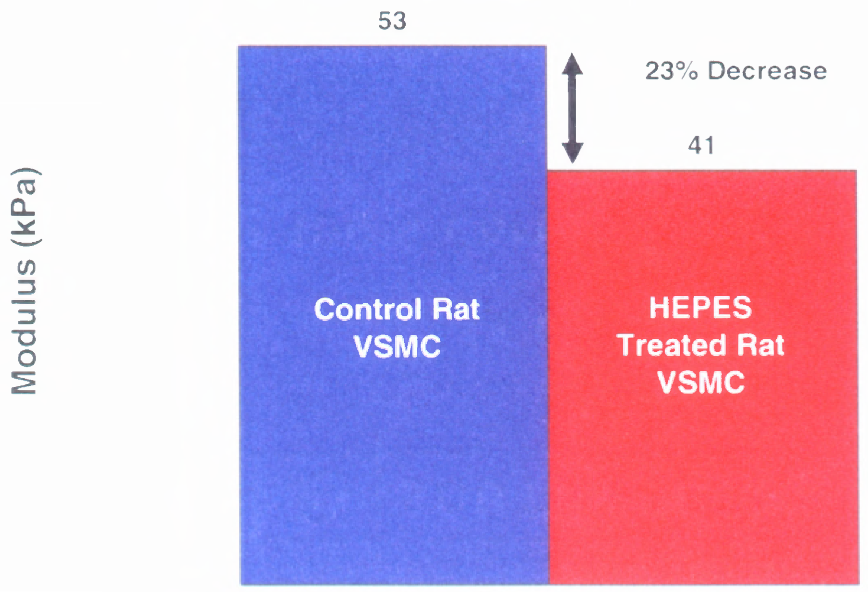

Figure 4.8 Comparison of the modulus of control and hepes treated rat VSMCs, where 23% decrease in E was seen after the application of HEPES

4.3 Comparison Of The Morphology And Moduli Of Old & Young Mouse VSMCs

Sample AFM images of the young (Date of Birth 1/9/2002) and old (Date of Birth 5/18/2000) mouse VSMC's are shown in Figure 4.9. The morphology change is seen in a smaller scan size of 30 μm (Figure 4.10). It is evident that the young and old VSMC have a different structure. The cell body height of the old cell was measured to be 456 nm, whereas the young cell body height was 363 nm. The increase in thickness was expected according to the physiology of the aging process. The aging process affects arterial stiffness by causing cell death reducing the number of VSMCs in the arteries. The remaining VSMC's are forced to work harder causing them to enlarge [2].

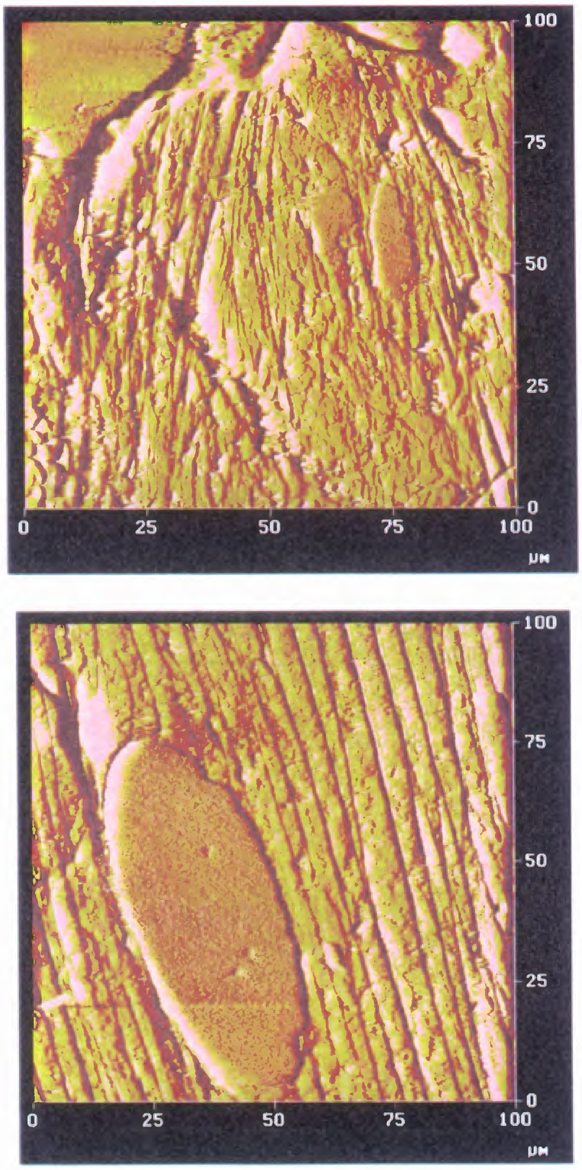

Figure 4.9 Comparison of the morphology of old (top) and young (bottom) mouse VSMCs at 100 µm scan size.

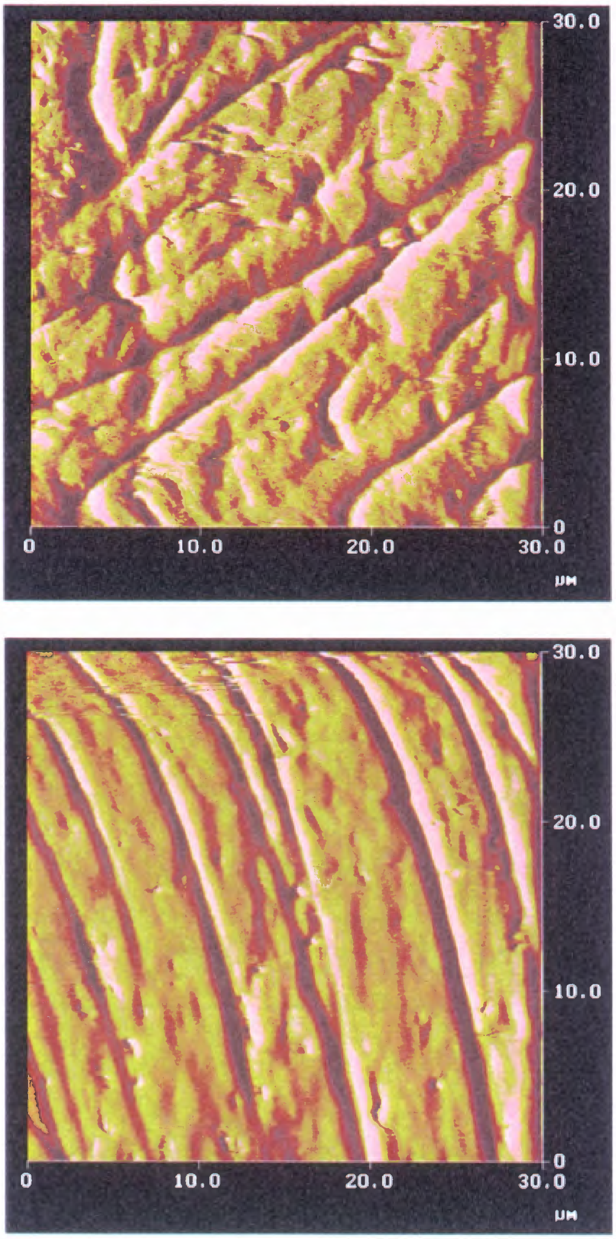

Figure 4.10 Comparison of the morphology of old (top) and young (bottom) mouse VSMCs at 30 μm scan size, demonstrating a difference in tissue morphology.

A Force (P) versus Distance Plot (D_z) was measured with the AFM. From this data a blunt cone indenter geometry was used to compare the Young's modulus for two young and old cells (Figure 4.10 & Table 4.1).

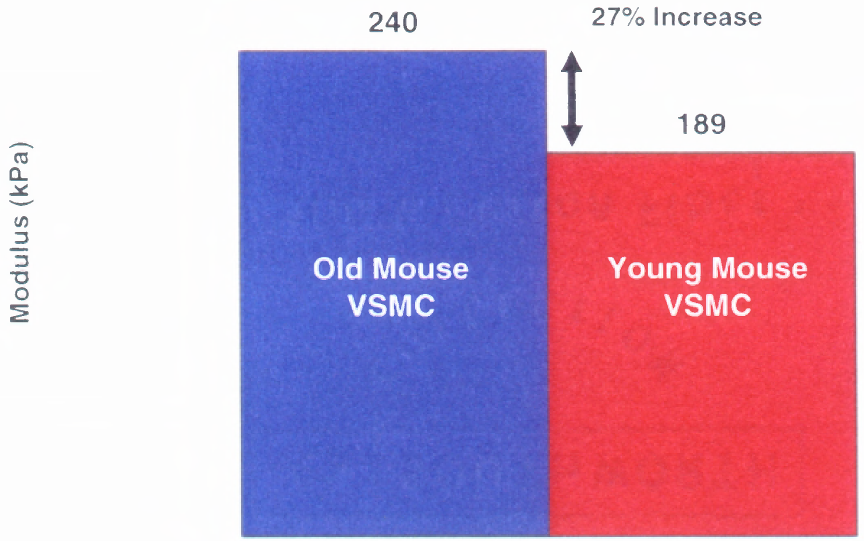

Figure 4.11 Comparison of the modulus of young and old mouse VSMCs, where a 27% increase in E was seen with age. The modulus was determined from an indentation of 100 nm representing 22% and 28% of the old and young cell body thickness respectively.

Table 4.1 Young's Modulus For Cells 1 & 2 In Young And Old Mice

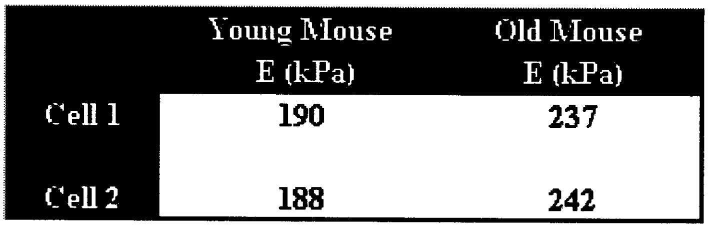

	Young Mouse E (kPa)	Old Mouse E (kPa)
Cell 1	190	237
Cell 2	188	242

The Young's modulus for the young mouse VSMC, is observed to be smaller than that of the old mouse VSMC by 27 %. These results are expected given the effect of aging on the arteries and how a change in morphology could lead to an increase in arterial stiffness [2]. Moreover, the average moduli values of 239 kPa and 189 kPa for the old and young VSMC cells are close to the range of values (0-200 kPa) noted by other researchers for biological material [41]. This result was confirmed with two trials; however, more trials are necessary to properly determine the effect of age on VSMC stiffness.

4.4 Detection of Cell Morphology Change With AFM Applied To Nocodazole Treated Rat VSMC's

There is increasing evidence that vascular stiffening due to aging can be slowed down by drugs [6]. We therefore applied nocodazole a reagent known to convert the normally polymeric α-tubulin in the cytoskeleton of the VSMC into monomers. This disruption of the cytoskeleton affects the mechanical properties of the VSMC. Figures 4.12 and 4.13 show the effect of nocodazole on the cytoskeleton of the rat VSMC's as imaged by the AFM.

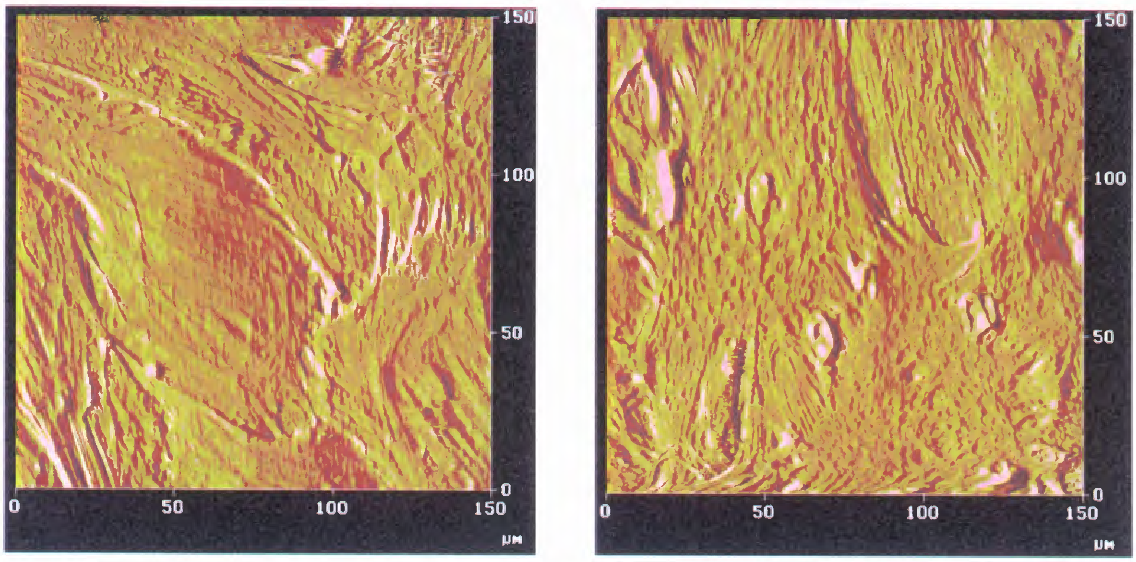

Control Rat VSMC

Nocodazole Treated Rat VSMC

150 μm AFM Scan Size

150 μm AFM Scan Size

Figure 4.12 The effect of nocodazole on the cytoskeleton of the rat VSMCs 150 μm scan.

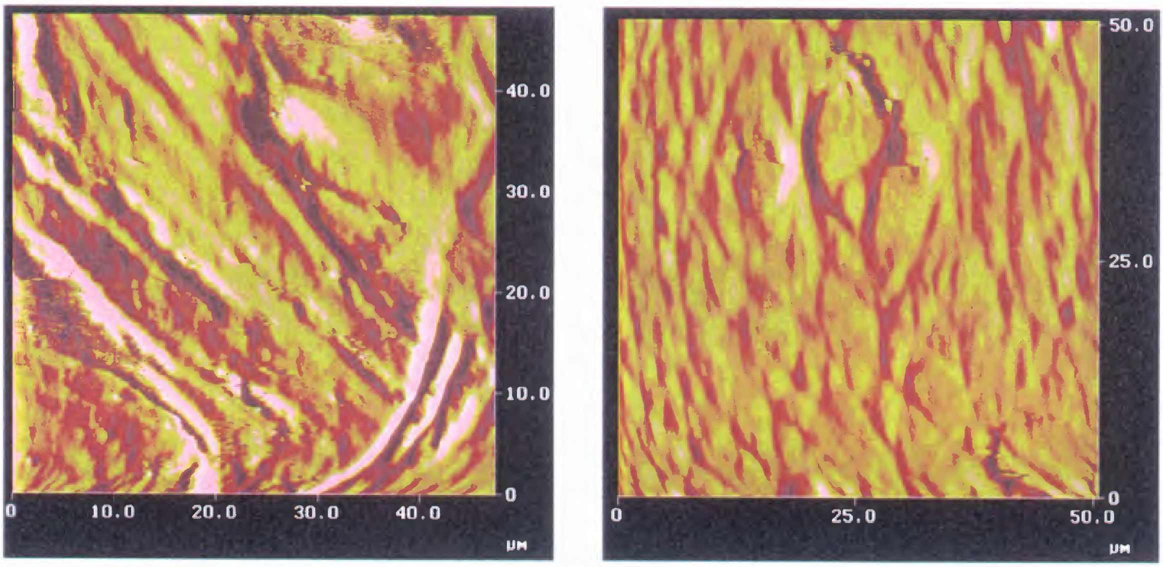

Control Rat VSMC

Nocodazole Treated Rat VSMC

50 μm AFM Scan Size

50 μm AFM Scan Size

Figure 4.13 The effect of nocodazole on the cytoskeleton of the rat VSMCs 50 μm scan.

Figures 4.12 and 4.13 clearly illustrate how the AFM can detect changes in cell morphology. More trials are necessary to determine the changes in mechanical properties resulting from drug treatment.

CHAPTER 5

CONCLUSIONS AND SUGGESTIONS

5.1 Conclusion

The age-related changes in vascular stiffness are risk factors for strokes and heart attacks [2]. The AFM enabled us to image the three-dimensional structure of VSMCs in their physiological environment allowing us to monitor their morphology and mechanical property changes. Indentations with a blunt cone indenter fit the force indentation data better than the conical indenter when applied to the classical infinitesimal theory. Therefore, a blunted cone model should be applied over the conical one when predicting a Young's modulus (E) from classical infinitesimal strain theory.

When HEPES buffer is added to the cultured VSMC, a morphology change is clearly seen. Moreover, the cell body height of the HEPES treated cell was measured by AFM to be 1 μm, whereas the non-treated cell body height was 424 nm. The Young's modulus (E) for the HEPES treated VSMC is smaller than that of the control by 23%. Therefore, the use of HEPES to control pH in cell culture should be reconsidered. The cell body height of the old cell was measured to be 456 nm, whereas the young cell body height was 363 nm. Moreover, the Young's modulus for the young mouse VSMC, was smaller than that of the old mouse VSMC by 27 %. The fact that the cell thickness and stiffness increases with age is expected [2]. However, the quantification of this increase has not been documented in the literature. The effect of Nocodazole on the cytoskeleton of the rat VSMC's was imaged by the AFM demonstrating that the morphology of rat VSMC can be altered by drug treatment which would lead to changes in VSMC mechanical properties. This adds more evidence that vascular stiffening due to aging can be slowed down by medication [6].

In summary, the blunted cone indenter geometry provides a better measurement of Young's modulus than a conical indenter in applications involving the classical infinitesimal strain theory. Moreover, these preliminary results have to be verified for reliability and accuracy. However, it is clear that the AFM is a powerful tool for gathering information on cells, and the application of classical infinitesimal strain theory with the proper indenter geometry could prove useful in comparative studies.

5.2 Suggestions

Future experiments should involve analysis of cell tissue viscoelasticity [4]. This could be accomplished by analyzing data from indentations occurring at different rates. A hydrodynamic drag should also be considered when interpreting AFM results. The drag can occur due to the viscous effects of the surrounding liquid [24,115,116], which adds a constant external force to the loading force of the cantilever. Electrostatic Coulomb interactions between charges on the specimen and tip (either occurring naturally or induced because of polarization), osmotic pressure due to charge movements and rearrangements, and structural forces such as hydration force, solvation force, and adhesion force should all be considered when imaging in fluids [25]. The cantilever's spring constant should also be determined experimentally in order to properly quantify the force applied to the cell.

AFM indentation of soft biological materials usually will not satisfy the conditions of infinitesimal strain theory because of the acute tip-angle of AFM probes, the tip dimensions, and typical sample thickness. To this end, it is important to determine whether the sample is a linear or nonlinear [74]. Costa's [74] results show that rather than simply fitting the entire force-depth curve, examining how the indentation response changes with depth can provide information about material nonlinearity. This should be incorporated in future analyses. Finally, a larger number of samples should be taken in order to assure reliability of data.

APPENDIX A

AFM FLUID CELL OPERATION

This section covers the use a fluid cell which consists of a small glass assembly with a wire clip for holding an AFM probe (Figure A.1).

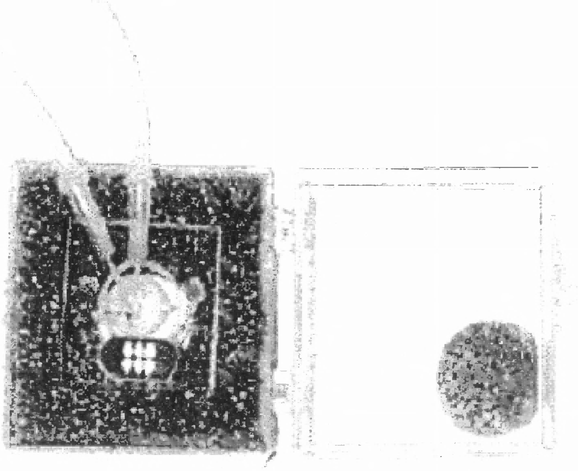

Figure A.1 Tapping Mode Fluid Cell in Case. Images Courtesy of Digital Instruments, Santa Barbara CA.

The glass surfaces provide a flat, beveled interface so that the AFM laser beam may pass into the fluid without being distorted by an unstable fluid surface (Fluid Cell Operation Information From Digital Instruments Support Note 290B Fluid Operation) [95].

A.1 Clean Fluid Cell and O-ring.

To reduce contamination problems and to obtain high-quality images, it is necessary to clean the fluid cell, and O-ring if applicable, in the following manner:

1. While soaking the fluid cell and O-ring in warm, soapy water, place a few drops of liquid dish soap on them.
2. Gently rub the fluid cell and O-ring with a cotton swab or finger. Avoid scratching the glass surface with abrasive material.
3. Using distilled water, rinse the fluid cell and O-ring of all soap.
4. Using 0.2 mm-filtered, compressed air or dry nitrogen, blow dry the fluid cell until all moisture evaporates.

A.2 Select the Probe

AFM probes featuring low stiffness cantilevers produce the best results for biological applications. Models NP-S (standard) or NP-STT (oriented twin tip) 100μm ("short"), V-shaped cantilevers with oxide-sharpened silicon nitride tips are recommended.

A.3 Remove Organic Contamination from the Probe Tip

Since contaminants on the probe tip may limit AFM resolution, it is necessary to use ultraviolet (UV) light to remove contaminants, in the following manner:

1. Place the fluid cell with installed tip face-up on a clean surface.
2. Position a UV lamp very close (3-5 mm) to the fluid cell and irradiate the probe for two minutes at full intensity.

A.4 Load the Fluid Cell with a Probe

The probe is held in a small pocket on the bottom side of the fluid cell by a gold plated, stainless steel wire clip. A tiny coil spring mounted on the top of the fluid cell holds the wire clip against the probe. Load a probe into the fluid cell by performing the following procedure:

1. Turn the fluid cell upside down, and gently raise the wire clip by pressing from beneath.
2. With the wire clip raised, use tweezers to slide a probe into the pocket. Lower the clip to hold the probe (Figure A.2).

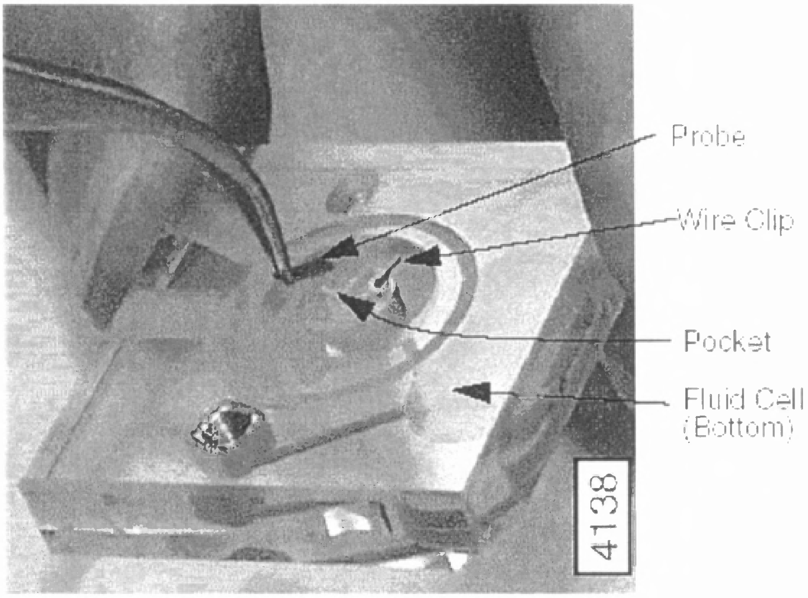

Figure A.2 Probe loaded into the fluid cell. Image courtesy of Digital Instruments, Santa Barbara CA.

3. Verify that the probe is squarely set against one side of the pocket and flush against the back. Verify the probe is held firmly by the wire.

A.5 Sample Mounting

Secure a 15mm glass sample slide containing cells to a magnetic stainless steel sample puck. Supports may be secured to the puck with epoxy (Fig. 3.5).

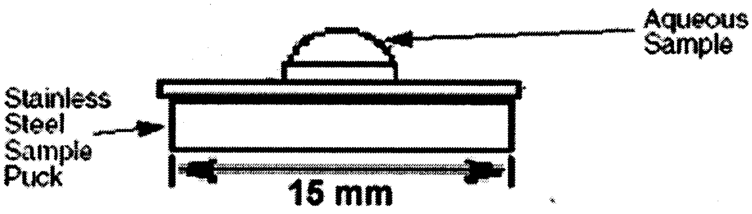

Figure A.3 Stainless-steel puck with aqueous sample image courtesy of Digital Instruments, Santa Barbara CA.

A.6 Method To Load Fluid Cell With Solution

A.6.1 Install The Protective O-Ring Into The Fluid Cell

1. Insert the O-ring into the recessed groove in the underside of the fluid cell. The O-ring slides up into the recessed groove.
2. Position the O-ring so that it forms a seal around its periphery and does not overlap any edges.

A.6.2 Pre-Wet The Fluid Cell (Figure A.4)

Occasionally, air bubbles form in the fluid cell and block laser light. Preventing bubbles from forming can be obtained by following the steps below:

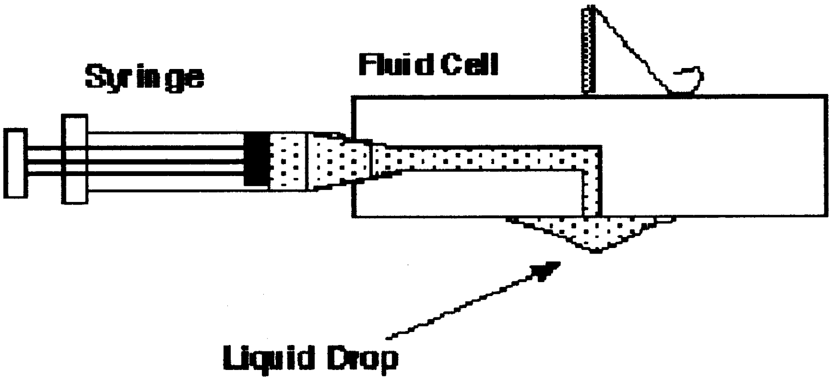

Figure A.4 Fluid inserted into the fluid cell. Sample image courtesy of Digital Instruments, Santa Barbara CA.

1. Before installing the fluid cell into the head, insert a syringe filled with liquid solution into a fluid port, or connect the syringe to the inlet tubing on the fluid cell.
2. Push enough fluid through the fluid chamber in order to flood the fluid cell port, allowing liquid to drip out of the bottom of the cell.
3. Leave the solution-filled syringe inserted. A small amount of solution should be held to the bottom of the cell by surface tension.

A.6.3 Install The Sample.

Install the sample attached to puck in the AFM head.

A.6.4 Install The Fluid Cell

Carefully install the fluid cell in the AFM head (Figure A.5).

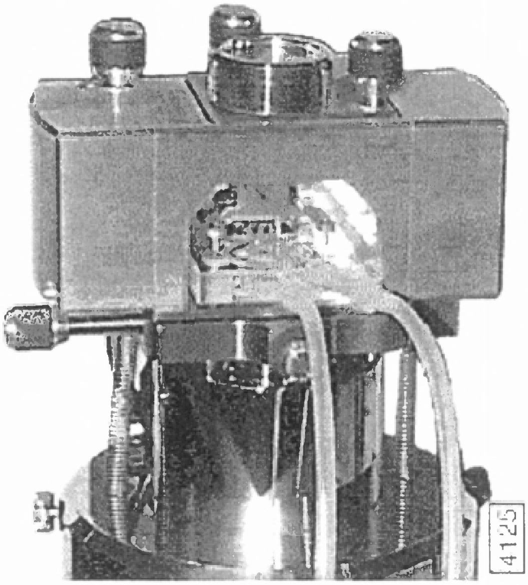

Figure A.5 Fluid cell inserted into AFM head. Sample image courtesy of Digital Instruments, Santa Barbara CA.

1. Tighten the clamp to hold the fluid cell in place, making certain that the O-ring positions properly between the sample and the fluid cell.
2. Verify the head is leveled side-to-side and that the head is tilted slightly forward, so the tip is leveled when it contacts the surface.
3. Fill the fluid cell with liquid. Limit the volume of liquid in the fluid cell to 30 – 50 μl, if possible, in order to limit thermal drift.
    a. Attach a drain line to the other fluid cell port.
    b. Slowly flush the fluid cell with solution from the syringe. Check for leaks and wipe away any spilled liquid with filter paper until the AFM components are dry.

4. Remove bubbles and clamp off fluid cell lines. Bubbles inside the fluid cell near or on the probe can interfere with the laser beam. Remove them by performing the following procedure:
    a. Observe the fluid cell and probe through the viewing port using an optical microscope.
    b. Rapidly push liquid through the cell with a syringe. If sufficient force is applied, the bubbles will be carried out of the fluid cell.
    c. Clamp off the drain line with a pair of hemostats or similar clamp.
5. Adjust the laser:
    a. If the presence of fluid causes the laser spot to refract, slightly adjust the laser aiming screw, to move the laser spot onto the end of the probe.
    b. If air bubbles become trapped near the probe, interfering with the laser beam path, use the syringe to force liquid quickly through the cell to break the bubbles loose.

A.7 Align the Laser

Use the x- and y- laser adjustment knobs to align laser spot onto the tip of the cantilever. Insert a small slip of paper into the laser beam path to perform fine laser alignment. Carefully adjust the laser adjustment knobs in both directions to achieve a solid rectangle bar-shaped pattern reflected onto the slip of paper.

A.8 Adjust the Detector Offsets and Setpoint (Contact Mode)

Turn the detector mirror adjustment screws to center the laser spot on the laser detector. For contact mode, set the vertical deflection signal to roughly -1.0 V and the setpoint to 0 V to begin. The difference between the vertical deflection signal before engaging and the setpoint determines the amount of force that the probe applies to the sample. Typically, samples are softer in liquid than in air. Before engaging, verify that there is not much difference between the setpoint and the vertical deflection signal as to damage the sample.

A.9 Engage the Surface

Using the coarse adjustment screws and MOTOR DOWN switch on the NanoScope® MultiMode™ ™ base, lower the tip until it is just above the level of the sample surface. In the Real Time / Motor menu, click ENGAGE, or click the Engage icon. The motor begins to move the AFM head and probe down to the sample. When the tip reaches the surface, the system should automatically stop, beep, and begin to image the sample.

A.10 Adjust Scan Parameters (Contact Mode)

Once engaged, adjust the scan parameters to obtain the best image as follows. To avoid sample damage, adjust the setpoint as low as possible:

1. Reduce the setpoint in increments of 1/100 volt.
2. Stop when the tip pulls off the surface and the Z Center Position on the display monitor jumps to Limit (-220 V).

3. Increase the setpoint until the tip begins to touch the surface again and an image appears.
4. Set the two gains as high as possible (starting with the integral gain) without causing oscillation distortion to appear in your image.
5. Choose a scan rate that is sufficiently slow to image without degrading your data.

A.11 Fluid Cell Operation In Tapping Mode

Operation of Tapping Mode in fluid provides the same advantages of TappingMode in air, with the additional ability to image samples under native liquid conditions. In fluid TappingMode, the probe is oscillated so that it only intermittently contacts the sample surface. This can reduce or eliminate lateral forces that can damage soft or fragile samples in contact mode.

A.11.1 Procedure for Tapping Mode Imaging in Fluid

1. Load the sample in the AFM.
2. Align the laser on the end of the cantilever portion of the probe.
3. Center the photodiode to give a deflection signal near 0V.
4. Choose the TappingMode operation in software.
5. Set the initial scan parameters, by entering the View/Sweep/Cantilever Tune menu to select a drive frequency and manually tune the probe using the Zoom in and Offset functions above the Cantilever Tune display.

6. Center the laser spot on the photodiode detector. Adjust the photodiode until deflection is roughly zero. The deflection signal can drift when the probe is first in fluid, so it is best to adjust just prior to engaging.
7. Click the Engage icon to bring the tip into tapping range.
8. Adjust the setpoint when engaged.

APPENDIX B

INFINITESIMAL INDENTATION SUPERPOSED ON A FINITE EQUIBIAXIAL STRETCH

This section covers the development of the formulas used related to the infinitesimal indentation by a rigid axisymmetric punch superposed on finite deformations of an elastic half-space for compressible and incompressible, isotropic, hyperelastic materials taken from the following sources [74,82-84,109]. Costa [74] presented the equations relating indentation force and depth for axisymmetric punch geometries based on Humphrey's work [84]considering incompressible materials indented by a flat-ended cylinder.

The following is the general equation for the total force (P) exerted by an indenter for infinitesimal indentations perpendicular to the finite stretch [74,83].

$$P = 2\cdot\pi\cdot\frac{\Gamma(W)}{\Sigma(W)}\cdot\phi(d) \qquad (B.1)$$

Where $\phi(d)$ is a function of the indenter geometry, which determines the dependence of P on the penetration depth (d). $\Gamma(W)$ and $\Sigma(W)$ incorporate the material properties and in-plane deformation through their dependence on the strain energy function, $W(I_1, I_2)$, and the principal strain invariants, I_1 and I_2. For finite equibiaxial stretch, μ, the deformation gradient tensor is $F=\mathrm{diag}\{\mu,\mu,\lambda\}$, where $\lambda=\mu^{-2}$ to satisfy material incompressibility. For incompressible materials Γ and Σ can be written as

$$\Gamma=\frac{\left(q_1\cdot k_1+q_2\right)\cdot\sqrt{k_1}}{1+k_1}-\frac{\left(q_1\cdot k_2+q_2\right)\cdot\sqrt{k_2}}{1+k_2}$$

$$\Sigma=\frac{k_1}{1+k_1}-\frac{k_2}{1+k_2} \qquad \text{(B.2)}$$

where k_1 and k_2 are roots of the following quadratic equation for K[84]

$$m\cdot K^2+(1+m-n-o)\cdot K+l=0 \qquad \text{(B.3)}$$

where

$$l=2\cdot\lambda^2\cdot\left(W_1+\mu^2\cdot W_2\right)$$

$$m=2\cdot\mu^2\cdot\left(W_1+\mu^2\cdot W_2\right)$$

$$n=4\cdot\mu^2\left[\left(W_1+\mu^2\cdot W_2\right)+(\mu^2-\lambda^2)\cdot\left[W_{11}+W_{22}\cdot\mu^2\cdot(\lambda^2+\mu^2)+W_{12}\cdot(\lambda^2+2\cdot\mu^2)\right]\right.$$

$$o=4\cdot\lambda^2\cdot\left[\left(W_1+\mu^2\cdot W_2\right)+(\lambda^2-\mu^2)\cdot\left(W_{11}+2\cdot W_{22}\cdot\mu^4+3\cdot W_{12}\cdot\mu^2\right)\right]$$

where W_{ij} (i, j=1, 2) are second derivatives of W with respect to I_i or I_j and

$$q_1=2\cdot\mu^2\cdot\left(W_1+\mu^2\cdot W_2\right) \qquad \text{(B.4a)}$$

$$q_2=2\cdot\lambda^2\cdot\left(W_1+\mu^2\cdot W_2\right) \qquad \text{(B.4b)}$$

Where W1 and W2 are derivatives of W with respect to I_1 and I_2 respectively [74].

The special case of zero in-plane stretch ($\mu=\lambda=1$ and $k_1=k_2=1$), yields $\Gamma=\Sigma=0$, such that Γ/Σ is indeterminate. This limit can be found by first setting $k_1=1$ in (B.2)

$$\left(\frac{\Gamma}{\Sigma}\right)_{k_1=1}=\frac{2\cdot l_1\cdot k_2+\left(l_1-l_2\right)\cdot\sqrt{k_2}+l_1+l_2}{\sqrt{k_2}+1} \tag{B.5}$$

with $k_2=1$ and (B.4a), yields

$$\lim_{\mu\to 1}\frac{\Gamma}{\Sigma}=4\cdot\left(W_1+W_2\right)_{\mu=1}=E_g \tag{B.6}$$

E_g is a generalized elastic modulus for any isotropic, incompressible, hyperelastic material in its unstretched state. Classical solutions for the infinitesimal indentation are expressed in terms of

$$E_c=\frac{E}{1-\nu^2} \tag{B.7}$$

E is Young's modulus and ν is Poisson's ratio. For incompressible materials ν is 0.5 [78]. For the case of linear hyperelastic materials, where $W_1=C_1$ and $W_2=C_2$ are constants, E_g from (B.6) is equal to 2/3 the Young's modulus given by $E=6(C1+C2)$ [74,117]. Equation (B.1) becomes

$$P=2\cdot\pi\cdot E_g\cdot\phi(d)=\frac{4}{3}\cdot E\cdot\pi\cdot\phi(d) \qquad (B.8)$$

Where d is the indentation depth measured from the free surface at the axis of symmetry. Costa's system [74] involves obtaining $\phi(d)$ from existing solutions to express them in the form of (B.8). Expressions for $\phi(d)$ for a rigid spherical and conical punch indenter geometries were developed because many of the axisymmetric punch shapes of principal interest can be described by a quadratic function [83].

$$f(r)=c_0+c_1\cdot r+c_2\cdot r^2 \qquad (B.9)$$

Where c_β, $\beta=0,1,2$, are constants determined from the assigned geometry. The radius of the circle of contact is a. The variable r describes the convex punch shape as the radial distance from the axis in the range $0\leq r\leq a$. From [83] we obtain a relation for $\phi(d)$.

$$\phi(r,a)=\left(a^2-r^2\right)^{\frac{1}{2}}\cdot\left[\frac{2\cdot c_0}{\pi}+\frac{1}{2}\cdot c_1\cdot\left[a+r^2\cdot\left(a^2-r^2\right)^{\frac{-1}{2}}\cdot\cosh^{-1}\left(\frac{a}{r}\right)\right]+\frac{4\cdot c_2}{3\cdot\pi}\cdot\left(a^2+2\cdot r^2\right)\right] \qquad (B.10)$$

When r =0, this expression reduces to

$$\phi(0,a)=a\cdot\left(\frac{2\cdot c_0}{\pi}+\frac{1}{2}\cdot c_1\cdot a+\frac{4\cdot c_2\cdot a^2}{3\cdot\pi}\right) \qquad (B.11)$$

Specific punch shapes can be determined with this relation.

Cone With Tip Angle, 2α [77,83]

The indentation of a conical punch of apex angle 2α may be described by

$$f(r)=d-r\cdot\cot(\alpha) \qquad \text{(B.12)}$$

where d denotes the maximum depth of indentation. Therefore,

$c_o=d$, $c_1=-\cot(\alpha)$, and $c_2=0$ in (B.11)

gives

$$\phi(0,a)=a\cdot\left(\frac{2\cdot d}{\pi}-\frac{1}{2}\cdot\cot(\alpha)\cdot a\right) \qquad \text{(B.13)}$$

The incremental stress should not become infinite at the ultimate circle of contact r=a. To this end,

$$\frac{d}{dr}\phi(r,a)$$

should be finite , therefore

$$2\cdot d=\pi\cdot a\cdot\cot(\alpha) \qquad \text{(B.14)}$$

Putting (B.14) into (B.13) gives

$$\phi(0,a)=a\cdot\left(\frac{\pi\cdot a\cdot\cot(\alpha)}{\pi}-\frac{1}{2}\cdot\cot(\alpha)\cdot a\right)$$

which simplifies to

$$\phi(d)=\frac{2\cdot\tan(\alpha)}{\pi^2}\cdot d^2 \tag{B.15}$$

This is the conical indenter geometry function.

Sphere With Radius, R [83]

The infinitesimal indentation by a spherical punch of radius R is characterized by

$$f(r)=d-\frac{r^2}{2\cdot R} \tag{B.16}$$

therefore

c_o=d, c_1=0, and c_2=-1/2R in (B.11) gives

$$\phi(0,a)=r_0\cdot\left(\frac{2\cdot d}{\pi}-\frac{2\cdot a^2}{3\cdot\pi\cdot R}\right) \tag{B.17}$$

In order that the incremental stress distribution [83] be finite at r=a, we must have

$$a^2 = R \cdot d \tag{B.18}$$

Inserting (B.18) into (B.17) we get

$$\phi(0,a) = \sqrt{R \cdot d} \cdot \left(\frac{2 \cdot d}{\pi} - \frac{2 \cdot R \cdot d}{3 \cdot \pi \cdot R} \right)$$

which simplifies to

$$\phi(d) = \frac{4}{3 \cdot \pi} \cdot \sqrt{R \cdot d^3} \tag{B.19}$$

This is the rigid spherical indenter geometry function.

Blunt Cone With Tip Angle 2α, Which Transitions At Radius R [109]

$\phi(d)$ for a blunt cone with tip angle 2α, which transitions at radius b into a spherical tip of radius R was examined with Briscoe's method [109].

The reciprocal theorem relates the P(d) function for any axisymmetric indenter, to the pressure distribution produced by a cylindrical punch of the same projected area as

$$P = \int_0^a \sigma(r) \cdot \frac{f(r)}{D} \cdot 2 \cdot \pi \cdot r \, dr \tag{B.20}$$

Where $\sigma(r)$ and D are the pressure distribution and depth of indentation respectively for the cylindrical punch, and f(r) is a function that specifies the indenter profile by its distance from the undeformed surface (d=0) as a function of the radial distance, r, from the axis $0 \le r \le a$. The pressure distribution under a perfect cylindrical punch is given by Sneddon [82]

$$\sigma(r) = \left(\frac{E_c}{\pi}\right) \cdot \frac{D}{\sqrt{a^2 - r^2}} \tag{B.21}$$

Substituting (B.21) into (B.20), we get

$$P = 2 \cdot E_c \cdot \int_0^a \frac{f(r) \cdot r}{\sqrt{a^2 - r^2}} \, dr \tag{B.22}$$

From Figure B.1 the function for a defective cone is

$$f(r) = d - \frac{r^2}{2 \cdot R} \qquad 0 \le a \le b \tag{B.23a}$$

$$f(r) = d - \frac{(r - b)}{\tan(\alpha)} - d_c \qquad d_c = \frac{b^2}{2 \cdot R} \qquad b \le a \tag{B.23b}$$

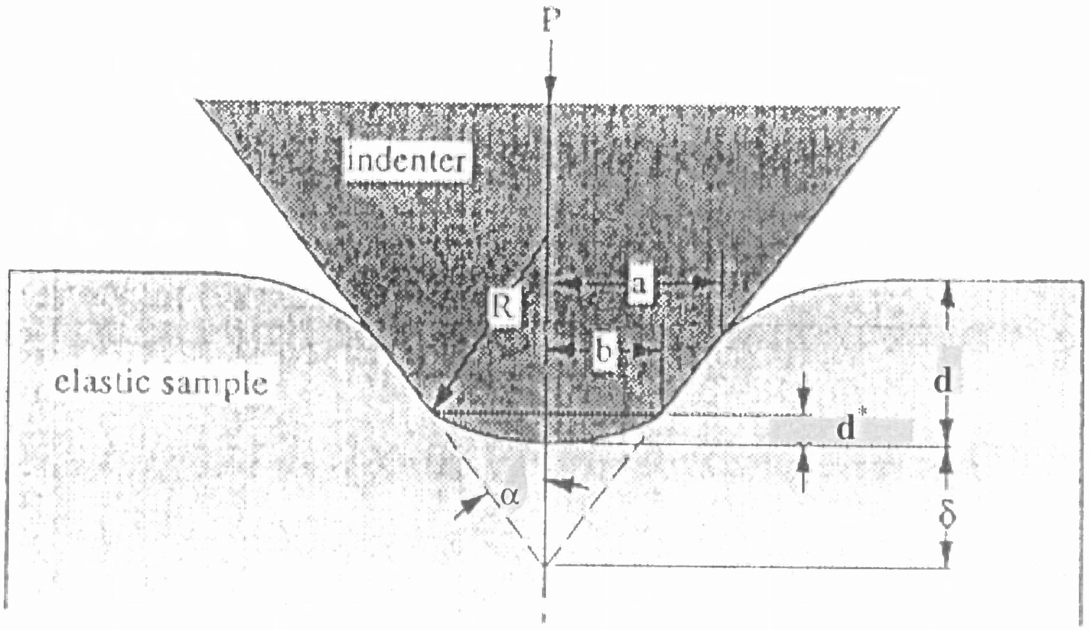

Figure B.1 A geometric model of a rigid cone with a spherical tip indenting an elastic half space [110].

When the spherical tip merges smoothly (tangential) with the body of the cone, the defect geometry is defined by R only and the corresponding value of b is given by b=Rcos(α).

When a≤b inserting (B.23a) into (B.22) gives

$$P=2\cdot E_c\cdot\int_0^a \frac{d-\frac{r^2}{2\cdot R}}{\sqrt{a^2-r^2}}\cdot r\,dr=2\cdot E_c\cdot\ a\cdot d-\frac{a^3}{3\cdot R} \qquad \text{(B.24)}$$

The radius of the contact zone is determined by maximizing the value of P with respect to a, that is, $\partial P/\partial a=0$, which results in $a=(Rd)^{1/2}$ and

$$P=\frac{4}{3}\cdot E_c\cdot\sqrt{R}\cdot d^{\frac{3}{2}}$$

The compliance equation for a sphere (Hertzian contact) where $\phi(d)$ is

$$\phi(d)=\frac{4}{3\cdot\pi}\cdot\sqrt{R\cdot d^3}$$

the rigid spherical indenter geometry function (B.19).

The depth of indentation corresponding to the transition from sphere indentation to (defective) cone indentation, d_s, is given by the boundary condition a=b; for which the value of d is $d_s=b^2/R=2d_c$.

The compliance equation when $a\geq b$

$$P=2\,E_c\cdot\left[\int_0^b \left(d-\frac{r^2}{2\cdot R}\right)\cdot\frac{r}{\sqrt{a^2-r^2}}\,dr+\int_b^a \left(d-\frac{r-b}{\tan(\alpha)}-d_c\right)\cdot\frac{r}{\sqrt{a^2-r^2}}\,dr\right]$$

$$P=2\cdot E_c\cdot\left[d\cdot\left[\int_0^a \frac{r}{\sqrt{a^2-r^2}}\,dr\right]-\left[\left(\frac{1}{\tan(\alpha)}\right)\cdot\int_a^b \frac{r^2}{\sqrt{a^2-r^2}}\,dr\right]-\left(\frac{1}{2\cdot R}\right)\cdot\int_0^b \frac{r^3}{\sqrt{a^2-r^2}}\,dr+\left(\frac{b}{\tan(\alpha)}-d_c\right)\cdot\int_b^a \frac{r}{\sqrt{a^2-r^2}}\,dr\right]$$

$$P=2\cdot E_c\cdot\left[a\cdot d-\frac{a^2}{2\cdot\tan(\alpha)}\cdot\left(\frac{\pi}{2}-\operatorname{asin}\left(\frac{b}{a}\right)\right)-\frac{a^3}{3\cdot R}+\sqrt{a^2-b^2}\cdot\left(\frac{b}{2\cdot\tan(\alpha)}+\frac{a^2-b^2}{3\cdot R}\right)\right] \qquad \text{(B.25)}$$

The condition $\partial P/\partial a=0$ applied to the above equation gives

$$d+\frac{a}{R}\cdot\left(\sqrt{a^2-b^2}-a\right)-\frac{a}{\tan(\alpha)}\cdot\left(\frac{\pi}{2}-\operatorname{asin}\left(\frac{b}{a}\right)\right)=0 \qquad \text{(B.26)}$$

Which is used to solve for the contact radius a. For $d<b^2/R$, $\phi(d)$ is given by (B.19) for a spherical indenter. When $d\geq b^2/R$, we have

$$\phi(d)=\frac{2}{\pi}\cdot\left[a\cdot d-\frac{a^2}{2\cdot\tan(\alpha)}\cdot\left(\frac{\pi}{2}-\operatorname{asin}\left(\frac{b}{a}\right)\right)-\frac{a^3}{3\cdot R}+\sqrt{a^2-b^2}\cdot\left(\frac{b}{2\cdot\tan(\alpha)}+\frac{a^2-b^2}{3\cdot R}\right)\right] \qquad \text{(B.27)}$$

REFERENCES

1. Lewis, R. (1998). *Life, 3rd Edition*, WCB/McGraw-Hill, New York.

2. Lakatta, E. G. (1998). *Vascular Disease in the Older Person*, CRC Press-Parthenon Publishers, New York.

3. Belz, G. G. (1995). "Elastic properties and Windkessel function of the human aorta." *Cardiovasc Drugs Ther.*, 9(1), 73-83.

4. Fung, Y. C. (1994). *Mechanical properties of living tissues*, Springer-Verlag, New York, NY.

5. Gaballa MA, J. C., Raya TE, Liu J, Simon B, Goldman S. (1998). "Large artery remodeling during aging: biaxial passive and active stiffness." *Hypertension*, 32, 437-43.

6. Van Bortel LM, S.-B. H., Safar ME. (2001). "Pulse pressure, arterial stiffness, and drug treatment of hypertension." *Hypertension*, 38, 914-21.

7. Cheng Zhu, G. B., and NingWang. (2000). "Cell Mechanics: Mechanical Response, Cell Adhesion, and Molecular Deformation." *Annu. Rev. Biomed. Eng.*, 02, 189–226.

8. Amos LA, A. W. (1991). *Molecules of the Cytoskeleton*, Guilford, New York.

9. Stossel, T. (1993). "On the crawling of animal cells." *Science*, 260, 1086-1094.

10. Ingber DE, D. L., Hansen L, Karp S, Liley H, et al. (1994). "Cellular tensegrity: exploring how mechanical changes in the cytoskeleton regulate cell growth, migration and tissue pattern during morphogenesis." *Int. Rev. Cytol.*, 150, 173-224.

11. Ingber DE, P. D., Sun Z, Betensky H, Wang N. (1995). "Cell shape, cytoskeletal mechanics, and cell cycle control in angiogenesis." *J. Biomech. Eng.*, 28, 1471-84.

12. Heidemann SR, B. R. (1994). "Mechanical tension as a regulator of axional development." *Neuro Toxicology*, 15, 95-108.

13. PA, J. (1998). "The cytoskeleton and cell signaling: component localization and mechanical coupling." *Physiol Rev.*, 78, 763-81.

14. Desai A, M. T. (1997). "Microtubule polymerization dynamics." *Ann Rev Cell & Develop Biol. 1997*, 13, 83-117.

15. Ingber, D. (1997). "Tensegrity: the architectural basis of cellular mechanotransduction." *Ann. Rev. Physiol. 1997*, 59, 575-99.

16. Wang N, B. J., Ingber DE. (1993). "Mechanotransduction across the cell surface and through the cytoskeleton." *Science*, 260, 1124-7.

17. HE., K. (1998). "Microtubules in cardiac hypertrophy: a mechanical role in decompensation?" *Circ Res.*, 82, 828-31.

18. Binnig, G. C. F. Q., and C. Gerber. (1986). "Atomic force microscope." *Phys. Rev. Lett.*, 56, 930-933.

19. Butt, H. J., E.K. Wolff, S.A.C. Gould, B.D. Northern, C.M. Peterson, and P.K. Hansma. (1990). "Imaging cells with the atomic force microscope." *J. Struct. Biol.*, 105, 54-61.

20. Chang L, K. T., Yorgancioglu M, Keller D, Pfeiffer J. (1993). "Cytoskeleton of living, unstained cells imaged by scanning force microscopy." *Biophys. J.*, 64(4), 1282-6.

21. E. Henderson, P. H. a. D. S. (1992). "Actin filament dynamics in living glial cells imaged by atomic force microscopy." *Science*, 257, 1944-1946.

22. Ezzell, W. H. G. a. R. M. (1996). "Viscoelasticity in Wild-Type and Vinculin-Deficient (5.51) Mouse F9 Embryonic Carcinoma Cells Examined by Atomic Force Microscopy and Rheology." *Exp. Cell Res.*, 226(1), 234-237.

23. Hofmann, U. G., Rotsch, C., Parak, W.J., and Radmacher, M. (1997). "Investigating the cytoskeleton of chicken cardiocytes with the atomic force microscope." *J. Struct. Biol.*, 119, 84-91.

24. M. Radmacher, M. F., CM Kacher, JP Cleveland and PK Hansma. (1996). "Measuring the visco-elastic properties of human platelets with the atomic force microscope." *Biophys. J.*, 70, 556-567.

25. Lal, R., and Scott A. John. (1994). "Biological applications of atomic force microscopy." *Am. J. Physiol.*, 266(Cell physiol. 35), C1-C21.

26. Jan Domke, W. J. P., Michael George, Hermann E. Gaub, and Manfred Radmacher. (1999). "Mapping the mechanical pulse of single cardiomyocytes with the atomic force microscope." *Eur. Biophys. J.*, 28(3), 179-186.

27. Dvorak JA, N. E. (1998). "Kinetic analysis of the mitotic cycle of living vertebrate cells by atomic force microscopy." *Exp Cell Res.*, 242(1), 69-74.

28. Hansma, H. G. a. J. H. H. (1994). "Biomolecular imaging with the atomic force microscope." *Annu Rev Biophys Biomol Struct 1994*, 23, 115-39.

29. SG Shroff, D. S. a. R. L. (1995). "Dynamic micromechanical properties of cultured rat atrial myocytes measured by atomic force microscopy." *Am. J. Physiol.*, 269, C286-C292.

30. Barbee, K. A., Davies, P.F. , and Lal, R. (1994). "Shear stress-induced reorganization of the surface topography of living endothelial cells imaged by atomic force microscopy." *Circ. Res.*, 74, 163-171.

31. Horber, J. K. H., W. Haberle, F. Ohnesorge, G. Binnig, H.G. Liebich, C.Z. Czerny, H. Mahnel, and A. Mayr. (1992). "Investigation of living cells in the nanometer regime with the scanning force microscope." *Scanning Microsc.*, 6, 919-930.

32. Kasas S, G. V., Celio MR. (1993). "Observation of living cells using the atomic force microscope." *Biophys. J.*, 64(2), 539-44.

33. Radmacher M, F. M., Kacher CM, Cleveland JP, Hansma PK. (1996). "Measuring the viscoelastic properties of human platelets with the atomic force microscope." *Biophysic J.*, 70, 556-67.

34. Barbee KA, M. T., Lal R, Davies PF. (1995). "Subcellular distribution of shear stress at the surface of flow-aligned and nonaligned endothelial monolayers." *Am. J. Physiol.*, 268, H1765-72.

35. Miyazaki H, H. K. (1999). "Atomic force microscopic measurement of the mechanical properties of intact endothelial cells in fresh arteries." *Med. Biol. Eng. Comput.*, 1999(4), 530-6.

36. Binnig, G., C. Gerber, E. Stoll, T.R. Albrecht, and C.F. Quate. (1987). "Atomic resolution with atomic force microscope." *Europhys. Lett.*, 3, 1281-1286.

37. M. Heuberger, G. D. a. L. S. (1994). "Mapping the Local Young's Modulus by Analysis of the Elastic Deformations Occurring in Atomic Force Microscopy." *Nanotechnology*, 5.

38. AL Weisenhorn, M. K., S Kasas, V Gotozos, MR Celio and HJ Butt. (1993). "Deformation and height anomaly of soft surfaces studied with the AFM." *Nanotechnology*, 4, 106-113.

39. Heuberger, M., Dietler, G. and Schlapbach, L. (1996). " J. Vac. Sci. Technol." B 14, 1250-1254.

40. J. Yang, J. M., J.Y. Yuan and Z. Shao. (1996). "The effect of deformation on the lateral resolution of atomic force microscopy." *J. Microsc.*, 182, 106-113.

41. Radmacher, M. (1997). "Measuring the elastic properties of biological samples with the AFM." *IEEE Eng. Med. Biol. Mag.*, 16, 47-57.

42. Persson, B. N. J. (1987). "The atomic force microscope: Can it be used to study biological molecules?" *Chem. Phys. Lett.*, 141(4), 366-368.

43. Lal, R., and L. Yu. (1993). "Molecular structure of cloned nicotinic acetyl choline receptors expressed in Xenopus oocyte as revealed by atomic force microscopy." *Proc. Natl. Acad. Sci. USA*, 90, 7280-7284.

44. Rotsch, C., and Radmacher, M. (2000). "Drug-Induced Changes of Cytoskeletal Structure and Mechanics in Fibroblasts: An Atomic Force Microscopy Study." *Biophys. J.*, 78, 520-535.

45. B. Drake, C. P., A.L. Weisenhorn, SAC Gould, TR Albrecht, et al. (1989). "Imaging crystals, polymers and biological processes in water with AFM." *Science*, 243, 1586-1589.

46. W. Haberle, J. H., F Ohnesorge, DPE Smith and G Binnig. (1992). "In situ investigations of living cells infected by viruses." *Ultramicroscopy*, 42-44, 1161-1167.

47. M Fritz, M. R. a. H. G. (1994). "Granula motion and membrane spreading during activation of human platelets imaged by atomic force microscopy." *Biophys. J.*, 66, 1328-1334.

48. Schoenenberger, J. H. a. C.-A. (1994). "Surface morphology and mechanical properties of MDCK monolayers by atomic force microscopy." *J. Cell Sci.*, 107, 1105-1114.

49. R Lal, B. D., D Blumberg, DR Saner, HG Hansma, and SC Feinstein. (1995). "Imaging real-time neurite outgrowth and cytoseletal reorganization with an atomic force microscope." *Am. J. Physiol.*, 269, C275-C285.

50. H Oberleithner, E. B., G Giebisch and J Geibel. (1995). "Visualizing life on biomembrane by atomic force microscopy." *Kidney International*, 48, 923-929.

51. M Beckmann, H.-A. K. a. F. L. (1994). "Atomic force microscopy of peritoneal macrophages after particle phagocytosis." *Membrane Biol.*, 140, 197-204.

52. Goodman, F. O. a. N. G. (1991). "Roles of the attractive and repulsive forces in atomic force microscopy." *Physical Rev. B*, 43, 4728-4731.

53. Butt, H. J. (1991). "Measuring electrostatic, van der Waals, and hydration forces in electrolyte solutions with an atomic force microscope." *Biophys. J.*, 60, 1438-1444.

54. Hoh, J. H., J.P. Cleveland, C.B. Prater, J.P. Revel, and P.K. Hansma. (1992). "Quantized adhesion detected with the atomic force microscope." *J. Am. Chem. Soc.*, 114, 4917-4918.

55. P.A. Janmey, S. H., J. Käs, D. Lerche, A. Maggs, E. Sackmann, M. Schliwa and T.P. Stossel. (1994). "The mechanical properties of actin gels. Elastic modulus and filament motions." *J. Biol. Chem.*, 269(51), 32503-32513.

56. Stryer, L. (1988). *Biochemistry, 3rd Edition*, W.H. Freeman and Company, New York.

57. Hartwig, J. (1991). "Actin-binding proteins." *Curr. Op. Cell. Biol.*, 3, 87-97.

58. Sackmann, E. (1994). "Intra- and extracellular macromoecular networks: physic and biological function." *Macromol. Chem. Phys.*, 195, 7-28.

59. Petersen NO, M. W., Elson EL. (1982). "Dependence of locally measured cellular deformability on position on the cell, temperature, and cytochalasin B." *Proc. Natl. Acad. Sci. USA*, 79, 5327-31.

60. Zahalak GI, M. W., Elson EL. (1990). "Determination of cellular mechanical properties by cell poking, with an application to leukocytes." *J. Biomech. Eng.*, 112, 283-94.

61. Evans E, Y. A. (1989). "Apparent viscosity and cortical tension of blood granulocytes determined by micropipet aspiration." *Biophys. J.*, 56, 151-60.

62. DE Discher, N. M. a. E. E. (1994). "Molecular maps of red cell deformation: hidden elasticity and in situ connection." *Science*, 266, 1032-1035.

63. K Zeman, H. E. a. E. S. (1990). "Bending undulations and elasticity of the erythrocyte membrane organization." *Europ. Biophys. J.*, 18, 203-219.

64. Dziedzic, A. A. a. J. (1989). "Internal cell manipulation using infrared laser traps." *Proc. Natl. Acad. Sci.*, 86, 7914-7918.

65. K Svoboda, C. S., D Branton and SM Block. (1992). "Conformation and elasticity of the isolated red blood cell membrane skeleton." *Biophys. J.*, 63, 784-793.

66. H Luers, K. H., J Litniewski and J Bereiter-Hahn. (1991). "Acoustic microscopy of cultured cells. Distribution of forces and cytoskeletal elements." *Cell Biophys.*, 18, 279-293.

67. Rugar, J. H. a. D. (1984). "Measurement of cellular elastic properties by acoustic microscopy." *J. Micros.*, 134, 245-260.

68. Pethica, J. B. O., W.C. (1987). "Tip surface interactions in STM and AFM." *Physica Scripta Volume T*, Volume T19A, 61-66.

69. Colton, N. B. a. R. J. (1989). "Measuring the nanomechanical properties and surface forces of materials using an atomic force microscope." *Journal of Vacuum Science & Technology A (Vacuum, Surfaces, and Films)*, 7(4), 2906-2913.

70. P. Maivald, H.-J. B., S.A.C. Gould, C.B. Prater, B. Drake, J.A. Gurley, V.B. Elings and P.K. Hansma. (1991). "Using force modulation to image surface elasticities with the atomic force microscope." *Nanotechnology*, 2(2), 103-106.

71. N.J. Tao, S. M. L. a. S. L. (1992). "Measuring the microelastic properties of biological material." *Biophysical Journal*, 63(4), 1165-1169.

72. A.L. Weisenhorn, P. K. H., T.R. Albrecht and C.F. Quate. (1989). "Forces in atomic force microscopy in air and water." *Appl. Phys. Lett.*, 54(26), 2651-2653.

73. B. Cappella, P. B., C. Frediani, P. Miccoli and C. Ascoli. (1997). "Force-distance curves by AFM. A powerful technique for studying surface interactions." *IEEE Eng. Med. Biol. Mag.*, 16(2), 58-65.

74. Costa, K. D. a. F. C. Y. (1999). "Analysis of indentation: implications for measuring mechanical properties with atomic force microscopy." *J Biomech Eng*, 121(5), 462-71.

75. Hertz, H. (1881). "Uber die beruhrung fester elastischer korper (On the contact of elastic solids)." *J. Reine Angew. Mathematik*, 92, 156-157.

76. Radmacher, M., Fritz, M., and Hansma, P.K. (1995). "Imaging soft samples with the atomic force microscope: Gelatin in water and propanol." *Biophys. J.*, 69, 264-270.

77. Love, A. E. H. (1939). "Boussinesq's problem for a rigid cone." *Q.J. Math.*, 10, 161-175.

78. Johnson, K. L. (1985). *Contact Mechanics*, Cambridge University Press, New York.

79. T.R. Albrecht, S. A., T.E. Carver and C.F. Quate. (1990). "Microfabrication of cantilever styli for the atomic force microscope." *J. Vac. Sci. Technol. A 8*, 8(4), 3386-3396.

80. Tortonese, M. (1997). "Cantilevers and tips for atomic force microscopy." *IEEE Eng. Med. Biol. Mag.*, 16, 28-33.

81. Vinckier, A. S., G. (1998). "Measuring elasticity of biological materials by atomic force microscopy." *FEBS Letters*, 430(1-2), 12-16.

82. Sneddon, I. N. (1965). "The Relation between load and penetration in the axisymmetric Boussinesq problem for a punch of arbitrary profile." *Int. J. Engng. Sci.*, 3, 47-57.

83. Beatty, M. F., and Usmani, S.A. (1975). "On the indentation of a highly elastic half-space." *Quart. J. Mech. Appl. Math.*, 28, 47-62.

84. Humphrey, J. D., Halperin, H.R., and Yin, F.C.P. (1991). "Small Indentation on a finite equibiaxial stretch: Implications for cardiac mechanics." *ASME Journal of Applied Mechanics*, 58, 1108-1111.

85. Hayes, W. C., Keer, L.M. (1972). "A mathematical analysis for indentation tests of articular cartilage." *J. Biomech. Eng.*, 5, 541-551.

86. Karduna, A. R., Halperin, H.R., and Yin, F.C.P. (1997). "Experimental and numerical analyses of indentation in finite-sized isotropic and anisotropic rubber-like materials." *Ann. Biomed. Eng.*, 25, 1009-1016.

87. J.P. Cleveland, S. M., D. Bocek and P.K. Hansma. (1993). "A nondestructive method for determining the spring constant of cantilevers for scanning force microscopy." *Rev. Sci. Instrum.*, 64(2), 403-405.

88. Stokey, W. F. (1996). *Shock and Vibration Handbook (Harris, C.M., Ed.), Ch. 7*, McGraw-Hill, New York.

89. Revel, J. A. D. a. J.-P. (1997). "Examination of atomic (scanning) force microscopy probe tips with the transmission electron microscope." *Microsc. Microanal.*, 3(3), 203-213.

90. S. Grafström, M. N., T. Hagen, J. Ackermann, R. Neumann, O. Ptobst and M. Wörtge. (1993). "The role of topography and friction for the image contrast in lateral force microscopy." *Nanotechnology*, 4(3), 143-151.

91. Hoh, C. S. a. J. (1994). "Slow cellular dynamics in MDCK and R5 cells monitored by time-lapse atomic force microscopy." *Biophys. J.*, 67, 929-936.

92. Kawabe J, A. Y., Takehara N, Hasebe N, Kikuchi K. (2000). "Glucose modifies the cross-talk between insulin and the beta-adrenergic signalling system in vascular smooth muscle cells." *J Hypertension.*, 18, 1457-64.

93. Aizawa Y, K. J., Hasebe N, Takehara N, Kikuchi K. (2001). "Pioglitazone enhances cytokineinduced apoptosis in vascular smooth muscle cells and reduces intimal hyperplasia." *Circulation*, 104, 455-60.

94. (1997). *MultiMode™ SPM instruction Manual Version 4.22ce*, Digital Instruments Incorporated Veeco Metrology Group, Santa Barbara, CA.

95. (1997). *MultiMode™ SPM Support Note 290-B FluidOperation*, Digital Instruments Incorporated Veeco Metrology Group, Santa Barbara, CA.

96. (1997). *MultiMode™ SPM Support Note 228-E Force Imaging*, Digital Instruments Incorporated Veeco Metrology Group, Santa Barbara, CA.

97. (1997). *MultiMode™ SPM Support Note No. 227, Rev. A Interpreting Force Image Data*, Digital Instruments Incorporated Veeco Metrology Group, Santa Barbara, CA.

98. White, J. E. S. a. E. (1994). "Theoretical analysis of the static deflection of plates for atomic force microscope applications." *Journal of Applied Physics*, 74(1), 1-9.

99. Sader, J. E. (1995). "Parallel Beam Approximation For V-Shaped Atomic Force Microscope Cantilevers." *Review of Scientific Instruments*, 66(9), 4583-4587.

100. G Chen, R. W., T Thundat et al. (1994). "Resonance Response of Scanning Force Microscopy Cantilevers." *Rev. Sci. Instrum.*, 65(8), 2532-2537.

101. G. Y. Chen, R. J. W. (1995). "Harmonic Response Of Near-Contact Scanning Force Microscopy." *Journal of Applied Physics*, 78(3), 1465-1469.

102. A. Tori, S. M., K. Hane et al. (1996). "A method for determining the spring constant of cantilevers for atomic force microscopy." *Meas. Sci. Technol.*, 7, 179-184.

103. Ducker, T. J. S. a. W. A. (1994). "Experimental Determination Of Spring Constants In Atomic Force Microscopy." *Langmuir*, 10(4), 1003-1004.

104. C. T. Gibson, G. S. W., and S. Myhra. (1996). "Determination Of The Spring Constants Of Probes For Force Microscopy/Spectroscopy." *Nanotechnology*, 7(3), 259-262.

105. J. E. Sader, I. L., P. Mulvaney et al. (1995). "Method For The Calibration Of Atomic Force Microscope Cantilevers." *Review of Scientific Instruments*, 66(7), 3789-3798.

106. Bechhoefer, J. L. H. a. J. (1993). "Calibration Of Atomic-Force Microscope Tips." *Review of Scientific Instruments*, 64(7), 1868-1873.

107. Manne, J. C. a. S. (1993). "A nondestructive method for determining the spring constant of cantilevers for scanning force microscopy." *Rev. Sci. Instrum.*, 64(2), 403-405.

108. Sarid, D. (1994). *Scanning Force Microscopy*, Oxford University Press, New York.

109. Briscoe, B. J., Sebastian, K.S., and Adams M.J. (1994). "The effect of indenter geometry on the elastic response to indentation." *J. Phys. D: Appl. Phys.*, 27, 1156-1162.

110. Gerald, C. a. W., P. (1997). *Applied Numerical Analysis*, Addison Wesley, New York.

111. Sato, M. N., K; Kataoka, N; Sasaki, M; Hane, K. (2000). "Local mechanical properties measured by atomic force microscopy for cultured bovine endothelial cells exposed to shear stress." *Journal of Biomechanics*, 33(1), 127-135.

112. Mathur AB, T. G., Reichert WM. (2000). "Atomic force and total internal reflection fluorescence microscopy for the study of force transmission in endothelial cells." *Biophys. J.*, 78(4), 1725-35.

113. Albrecht, T. R., Akamine, S. , Carver, T.E. and Quate, C.F. (1990). "Microfabrication of cantilever styli for the atomic force microscope." *J. Vac. Sci. Technol. A 8*, 8(4), 3386-3396.

114. Wood CM, P. P. (2000). "Intracellular pH regulation and buffer capacity in CO2/HCO3-buffered media in cultured epithelial cells from rainbow trout gills." *J. Comp. Physiol. [B]*, 170(3), 175-84.

115. Engel, J. H. a. A. (1993). "Friction Effects on Force Measurements with an Atomic-Force Microscope." *Langmuir*, 9(11), 3310-3312.

116. M. Radmacher, M. F., J.P. Cleveland, D.A. Walters and P.K. Hansma. (1994). "Imaging adhesion forces and elasticity of lysozyme adsorbed on mica with the atomic force microscope." *Langmuir*, 10(10), 3809-3814.

117. Green, A. E., and Zerna, W. (1968). *Theoretical Elasticity*, Oxford University Press, London.